

Soil Moisture Active and Passive Mission  
(SMAP)  
L1B\_S0, L1C\_S0  
Algorithm Theoretical Basis Document  
(ATBD)

R. West

October 27, 2014

# Contents

<b>1</b>	<b>Introduction</b>	<b>1</b>
<b>2</b>	<b>Mission and Instrument Overview</b>	<b>1</b>
2.1	Background and Science Objectives . . . . .	1
2.2	Measurement Approach . . . . .	2
2.3	L1 Processing Requirements . . . . .	6
<b>3</b>	<b>L0 Processing</b>	<b>6</b>
<b>4</b>	<b>L1 Processing Flow and Algorithm Interfaces</b>	<b>8</b>
4.1	Sources of Data . . . . .	8
4.1.1	Geometry Data . . . . .	8
4.1.2	Instrument Data . . . . .	10
4.1.3	Processing Parameters . . . . .	10
4.2	Output Data . . . . .	10
4.2.1	L1B Product Description . . . . .	10
4.2.2	L1C Product Description and Swath Grid . . . . .	12
4.3	Bit Flags in L1B and L1C products . . . . .	13
<b>5</b>	<b>Data Characteristics and Radar Performance</b>	<b>17</b>
5.1	Radar Resolution . . . . .	17
<b>6</b>	<b>Point Target Response and Time Range Definitions</b>	<b>23</b>
6.1	Radar RF Signal Generation . . . . .	23
6.2	Basebanded Point Target Response . . . . .	26
6.3	Forward and Backward Swath Row Time Range . . . . .	28
6.4	Forward and Backward Looks Time Ranges . . . . .	30
6.5	Synthetic Aperture Time . . . . .	30
6.6	Impulse Response Time . . . . .	31
<b>7</b>	<b>L1C Processing Algorithms</b>	<b>31</b>
7.1	Image Formation Theoretical Background . . . . .	31
7.2	High Level Algorithm Organization and the Direct Correlation Algorithm . . . . .	33
7.3	BFPQ Decoding . . . . .	35
7.4	Geometry Processing and Interpolation . . . . .	35
7.5	Range Compression . . . . .	37
7.5.1	RFI . . . . .	37
7.6	Azimuth Phase Correction . . . . .	37
7.7	Azimuth Compression . . . . .	38

7.8	Terrain-Corrected Geolocation . . . . .	39
7.9	Image Calibration using Radar Equation . . . . .	41
7.10	Regridding and Multi-Looking . . . . .	41
<b>8</b>	<b>L1B Processing Algorithms</b>	<b>42</b>
8.1	Noise Subtraction . . . . .	44
8.2	Radar Equation Scaling . . . . .	44
8.2.1	Scan Loss . . . . .	45
<b>9</b>	<b>Calibration</b>	<b>45</b>
9.1	Antenna Gain Pattern . . . . .	47
9.2	Receiver Gain and Noise Temperature . . . . .	47
9.3	Statistical Measurement Uncertainty and Noise Subtraction . . . . .	47
9.4	Radar Equation and Error Budget . . . . .	48
9.5	Long Term Detrending . . . . .	51
9.6	Absolute Calibration . . . . .	53
<b>10</b>	<b>Faraday Rotation</b>	<b>55</b>
<b>11</b>	<b>RFI</b>	<b>60</b>
11.1	Ground-Based Sources . . . . .	60
11.1.1	Impact of ground-based RFI contamination . . . . .	61
11.1.2	Detection and correction of ground-based RFI . . . . .	61
11.2	Space-Based RFI Sources . . . . .	62
11.2.1	Backlobe Contamination . . . . .	62
11.2.2	Reflection off the Earth . . . . .	62
11.3	Summary of RFI Error Assessment . . . . .	63
11.4	Baseline RFI Removal Algorithm . . . . .	63
<b>12</b>	<b>Validation and Test Procedures</b>	<b>64</b>
12.1	Pre-Launch . . . . .	64
12.1.1	Resolution Validation . . . . .	64
12.1.2	Radiometric Accuracy Validation . . . . .	65
12.1.3	Geolocation Validation . . . . .	65
12.2	Post-Launch . . . . .	65
12.2.1	Resolution and Signal Processing Validation . . . . .	66
12.2.2	Radiometric Accuracy Validation . . . . .	66
12.2.3	Geolocation Validation . . . . .	67
<b>13</b>	<b>Acknowledgments</b>	<b>67</b>
<b>14</b>	<b>Acronym List</b>	<b>68</b>

# 1 Introduction

This document describes the processing algorithms used by the SMAP ground system to compute radar backscatter ( $\sigma_0$ ) products along with the relevant system characteristics. There are two L1 products: the L1B\_S0 product which contains time ordered low resolution (6 km by 40 km)  $\sigma_0$  results, and the L1C\_S0 product which contains spatially gridded 1-km resolution  $\sigma_0$  results. The algorithms producing these two products are closely related and both are described in this document. The next section provides background about the SMAP Mission, the science requirements, and the derived instrument functional requirements. The third section briefly summarizes the L0 processing that will occur before L1 processing. The 4th section describes the high level processing flow and the layout of the L1 data products. The 5th section describes some of the special characteristics of the SMAP data. The 6th section describes the details of the radar data and the point target response which plays a central role in SAR processing. The next section describes the L1C processing algorithms. Included here are both algorithmic details and some software architecture details that are important to understanding how the L1C processor will work. The 8th section describes the calibration processes that will be applied and summarizes the error budget for the primary output of L1 processing, the normalized radar backscattering cross-section ( $\sigma_0$ ). The next section describes the baseline algorithm for dealing with RFI. Section 10 describes the testing and validation procedures that are planned.

## 2 Mission and Instrument Overview

### 2.1 Background and Science Objectives

The National Research Council's (NRC) Decadal Survey, Earth Science and Applications from Space: National Imperatives for the Next Decade and Beyond, was released in 2007 after a two year study commissioned by NASA, NOAA, and USGS to provide them with prioritization recommendations for space-based Earth observation programs [1]. Factors including scientific value, societal benefit and technical maturity of mission concepts were considered as criteria. SMAP data products have high science value and provide data towards improving many natural hazards applications. Furthermore SMAP draws on the significant design and risk-reduction heritage of the Hydrosphere State (Hydros) mission [2]. For these reasons, the NRC report placed SMAP in the first tier of missions in its survey. In 2008 NASA announced the formation of the SMAP project as a joint effort of NASA's Jet Propulsion Laboratory (JPL) and Goddard Space Flight Center (GSFC), with project management responsibilities at JPL. The target launch date is October

2014 [3].

The SMAP science and applications objectives are to:

- Understand processes that link the terrestrial water, energy and carbon cycles;
- Estimate global water and energy fluxes at the land surface;
- Quantify net carbon flux in boreal landscapes;
- Enhance weather and climate forecast skill;
- Develop improved flood prediction and drought monitoring capability.

## 2.2 Measurement Approach

Table 1 is a summary of the SMAP instrument functional requirements derived from its science measurement needs. The goal is to combine the attributes of the radar and radiometer observations (in terms of their spatial resolution and sensitivity to soil moisture, surface roughness, and vegetation) to estimate soil moisture at a resolution of 10 km, and freeze-thaw state at a resolution of 1-3 km.

The SMAP instrument incorporates an L-band radar and an L-band radiometer that share a single feedhorn and parabolic mesh reflector. As shown in Figure 1 the reflector is offset from nadir and rotates about the nadir axis at 14.6 rpm (nominal), providing a conically scanning antenna beam with a surface incidence angle of approximately  $40^\circ$ . The provision of constant incidence angle across the swath simplifies the data processing and enables accurate repeat-pass estimation of soil moisture and freeze/thaw change. The reflector has a diameter of 6 m, providing a radiometer 3 dB antenna footprint of 40 km (root-ellipsoidal-area). The real-aperture radar footprint is 30 km, defined by the two-way antenna beamwidth. The real-aperture radar and radiometer data will be collected globally during both ascending and descending passes.

To obtain the desired high spatial resolution the radar employs range and Doppler discrimination. The radar data can be processed to yield resolution enhancement to 1-3 km spatial resolution over the 70% outer parts of the 1000 km swath. Data volume prohibits the downlink of the entire radar data acquisition. Radar measurements that allow high-resolution processing will be collected during the morning overpass over all land regions and extending one swath width over the surrounding oceans. During the evening overpass data poleward of  $45^\circ$  N will be collected and processed as well to support robust detection of landscape freeze/thaw transitions.

The baseline orbit parameters are:

- Orbit Altitude: 685 km (2-3 days average revisit and 8-days exact repeat)

Table 1: SMAP Mission Requirements

Scientific Measurements	Measurement Requirements	Instrument Functional Requirements
Soil Moisture:	$\pm 0.04 m^3 m^{-3}$ volumetric accuracy (1-sigma) in the top 5 cm for vegetation water content $\leq 5 kg m^{-2}$ ; Hydrometeorology at 10 km resolution; Hydroclimatology at 40 km resolution	L-Band Radiometer (1.41 GHz): Polarization: V, H, T3 and T4 Resolution: 40 km Radiometric Uncertainty*: 1.3 K L-Band Radar (1.26 and 1.29 GHz): Polarization: VV, HH, HV (or VH) Resolution: 10 km Relative accuracy*: 0.5 dB (VV and HH) Constant incidence angle** between $35^\circ$ and $50^\circ$
Freeze/Thaw State:	Capture freeze/thaw state transitions in integrated vegetation-soil continuum with two-day precision, at the spatial scale of land-scape variability (3 km).	L-Band Radar (1.26 GHz and 1.29 GHz): Polarization: HH Resolution: 3 km Relative accuracy*: 0.7 dB (1 dB per channel if 2 channels are used) Constant incidence angle** between $35^\circ$ and $50^\circ$
Sample diurnal cycle at consistent time of day (6am/6pm Equator crossing); Global, 3 day (or better) revisit; Boreal, 2 day (or better) revisit		Swath Width: 1000 km Minimize Faraday rotation (degradation factor at L-band)
Observation over minimum of three annual cycles Includes precision and calibration stability ** Defined without regard to local topographic variation		Baseline three-year mission life

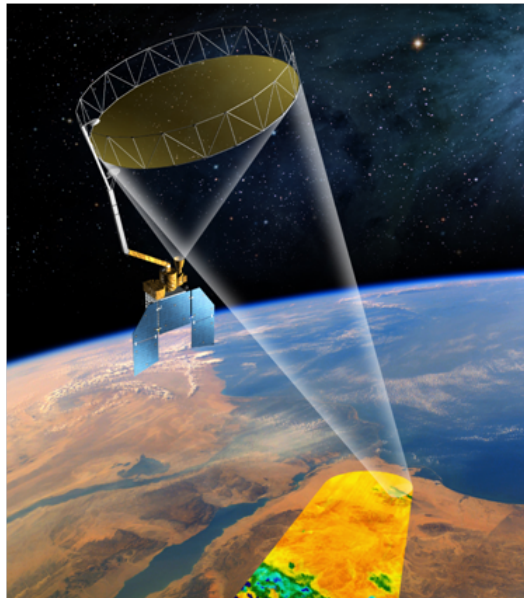


Figure 1: The SMAP observatory is a dedicated spacecraft with a rotating 6-m light-weight deployable mesh reflector. The radar and radiometer share a common feed.

- Inclination: 98 degrees, sun-synchronous
- Local Time of Ascending Node: 6 pm

The SMAP radiometer measures the four Stokes parameters, V, H and T3, and T4 at 1.41 GHz. The T3-channel measurement can be used to correct for possible Faraday rotation caused by the ionosphere, although such Faraday rotation is minimized by the selection of the 6am/6pm sun-synchronous SMAP orbit.

At L-band anthropogenic Radio Frequency Interference (RFI), principally from ground-based surveillance radars, can contaminate both radar and radiometer measurements. Early measurements and results from the SMOS mission indicate that in some regions RFI is present and detectable. The SMAP radar and radiometer electronics and algorithms have been designed to include features to mitigate the effects of RFI. To combat this, the SMAP radar utilizes selective filters and an adjustable carrier frequency in order to tune to pre-determined RFI-free portions of the spectrum while on orbit. The SMAP radiometer will implement a combination of time and frequency diversity, kurtosis detection, and use of T4 thresholds to detect and where possible mitigate RFI.

The SMAP planned data products are listed in Table 2. Level 1B and 1C data products are calibrated and geolocated instrument measurements of surface radar

Table 2: SMAP Data Products Table

Product	Description	Gridding (Resolution)	Latency	
L1A_TB	Radiometer Data in Time-Order	-	12 hrs	Instrument Data
L1A_S0	Radar Data in Time-Order	-	12 hrs	
L1B_TB	Radiometer $T_B$ in Time-Order	(36x47 km)	12 hrs	
L1B_S0_LoRes	Low Resolution Radar $\sigma_o$ in Time-Order	(5x30 km)	12 hrs	
L1C_S0_HiRes	High Resolution Radar $\sigma_o$ in Half-Orbits	1 km (1-3 km)	12 hrs	
L1C_TB	Radiometer $T_B$ in Half-Orbits	36 km	12 hrs	
L2_SM_A	Soil Moisture (Radar)	3 km	24 hrs	Science Data (Half-Orbit)
L2_SM_P	Soil Moisture (Radiometer)	36 km	24 hrs	
L2_SM_AP	Soil Moisture (Radar + Radiometer)	9 km	24 hrs	
L3_FT_A	Freeze/Thaw State (Radar)	3 km	50 hrs	Science Data (Daily Composite)
L3_SM_A	Soil Moisture (Radar)	3 km	50 hrs	
L3_SM_P	Soil Moisture (Radiometer)	36 km	50 hrs	
L3_SM_AP	Soil Moisture (Radar + Radiometer)	9 km	50 hrs	
L4_SM	Soil Moisture (Surface and Root Zone)	9 km	7 days	Science Value-Added
L4_C	Carbon Net Ecosystem Exchange (NEE)	9 km	14 days	

backscatter cross-section and brightness temperatures derived from antenna temperatures. Level 2 products are geophysical retrievals of soil moisture on a fixed Earth grid based on Level 1 products and ancillary information; the Level 2 products are output on half-orbit basis. Level 3 products are daily composites of Level 2 surface soil moisture and freeze/thaw state data. Level 4 products are model-derived value-added data products that support key SMAP applications and more directly address the driving science questions.

### **2.3 L1 Processing Requirements**

The SMAP Mission requirements are translated into requirements on the various spacecraft and instruments systems, including the L1 processing system. Table 3 lists the most important requirements that the L1 processing system has to meet. These requirements fall into three general categories: resolution requirements (eg., L3-MS-338,344), accuracy requirements - radiometric and spatial location (eg., L3-MS-371,353), and latency or throughput requirements (eg., L3-MS-312).

## **3 L0 Processing**

Although this ATBD focuses on the L1 processing algorithms, a few details about L0 processing are relevant. Data downlinks occur over downlink stations and produce raw telemetry files without any overlap. These files (designated L0a) are not quite ready for L1 processing. The L1 processing flow discussed in the next section expects half-orbit data granules with boundaries near the poles as input. The input granules are assumed to be complete, including all data that contributes to a half-orbit. Thus, there will be overlap of these input files (designated L0b) because of the conical scan used by SMAP. As the spacecraft approaches the northern most point in the ascending portion of an orbit, the conical scan will cover areas ahead that are needed in the subsequent descending portion of the orbit, and behind that are still needed to process the current ascending orbit. After passing the northern most point and starting southward in the following descending orbit section, the spacecraft will continue to collect data needed in the previous ascending orbit section as long as the backward parts of the conical scan extend across the northern most point. The half-orbit L0b granules will be formed so that they contain all data that contributes to a given ascending (or descending) half-orbit section. This means that sequential L0b files will contain some duplicated data that corresponds to the time it takes for the spacecraft to fly over one conical scan width. Depending on the availability of downlink stations, two L0a files, and occasionally three or more will contribute to one L0b granule. The splitting/merging needed to form the L0b half orbit input granules will be performed by a L0b preprocessor in coordination with

Table 3: Requirements applicable to L1 Processing

Requirement Number	Description
L3-MS-311	The Mission System shall ensure less than 7% data loss from instrument output through L-1 science product generation, including space-ground link losses.
L3-MS-383	The MS shall make available (to the project teams and DAAC) all L0b and L1 products within 2 hours (average mean latency over the mission) of availability of the L0a data at SDS for those products for which the complete orbit data has been received. (TBC)
L3-MS-338	The MS shall provide a calibrated "Hi-Res" radar sigma-0 Level 1C product at 3 km or better spatial resolution on a 1 km grid posting.
L3-MS-339	The MS shall provide a calibrated "Lo-Res" radar sigma-0 Level 1B product at 30 km x 6 km spatial resolution.
L3-MS-342	The MS shall process radar co-polarized horizontal (HH) and vertical (VV), and cross-polarized (HV) backscatter cross-sections.
L3-MS-386	The MS shall produce the L1C_S0_HiRes data product on a 1km grid.
L3-MS-344	The MS shall produce the L1C_S0_HiRes data product with a 3 km or less spatial resolution.
L3-MS-371	The MS shall produce the L1C_S0_HiRes data product with sigma0 error of 1 dB or less (1-sigma) in the HH and VV channels, for radar cross-sections (sigma-0) of -25 dB or greater; and TBD for the HV channel, including instrument precision, bias-removed calibration error, and RFI-induced error.
L3-MS-312	The MS shall make Level 1 data products available to the Science Team with a mean latency for the mission of twelve (12) hours of the corresponding data acquisition by the observatory under normal operating conditions.
L3-MS-364	The MS shall begin to make the validated Level 1 data available to the DAAC for public release within the first six (6) months of the science mission (Level 1 Cal/Val period).
L3-MS-373	After the initial release as defined in L3-MS-364, the MS shall make Level 1 data products available to the DAAC with a mean latency for the mission of twelve (12) hours of the corresponding data acquisition by the observatory under normal operating conditions.
L3-MS-353	The MS shall produce the L1C_S0_HiRes data product with geolocation errors of 1 km or less.

the operational process control system.

## 4 L1 Processing Flow and Algorithm Interfaces

Figure 2 shows a schematic diagram of the processing modules and data flow relationships for the level 0 and level 1 SMAP radar processing.

### 4.1 Sources of Data

The primary input to the L1A processor will be a L0b file containing EDOS data records. Data downlinked from the spacecraft includes spacecraft packetization. Most of the packetization will be removed by EDOS processing or by the L0b pre-processor. The radar data records embedded in the EDOS file structure will follow the format specified in the instrument telemetry dictionary. A L1A processor will unpack the L0b file, assembling radar records as needed and decode the raw telemetry data. Decoding includes all the necessary bit-level decoding and conversion of fields to floating point values with standard SI units where needed. Each record of the resulting L1A file contains data from one pulse repetition interval (PRI) when the instrument is in high-resolution mode, and from one 48-PRI long low-resolution interval when the instrument is operating in low-resolution mode. The block floating point quantized (BFPQ) encoded high-resolution samples are left unchanged at this stage so that diagnostic tools can examine the raw data using the L1A file. The L1A file is stored in HDF format and will be submitted for archival storage along with the output data products. The L1A file becomes the primary input to several processing modules including the L1B (low resolution) processor, the L1C (SAR) processor, and various diagnostic and support tools. In addition to the radar telemetry data, these processors will also require ancillary data to support geolocation and calibration. The ancillary data needed fall into three general groups - geometry data, instrument data, and processing parameters.

#### 4.1.1 Geometry Data

Processing SAR data and locating it on the surface will require precise data on the location of the spacecraft (ephemeris file), the attitude of the spacecraft and of the spinning antenna (ckernel file plus telemetry data), and the topography of the Earth (topographic data file). Ephemeris and ckernel files will be supplied by the navigation element of the project in coordination with the Navigation and Ancillary Information Facility (NAIF) at JPL. NAIF provides these data in standardized files called kernel files. There are 5 basic types of kernel files: S-kernels which contain spacecraft ephemeris data as a function of time, P-kernels which contain planetary

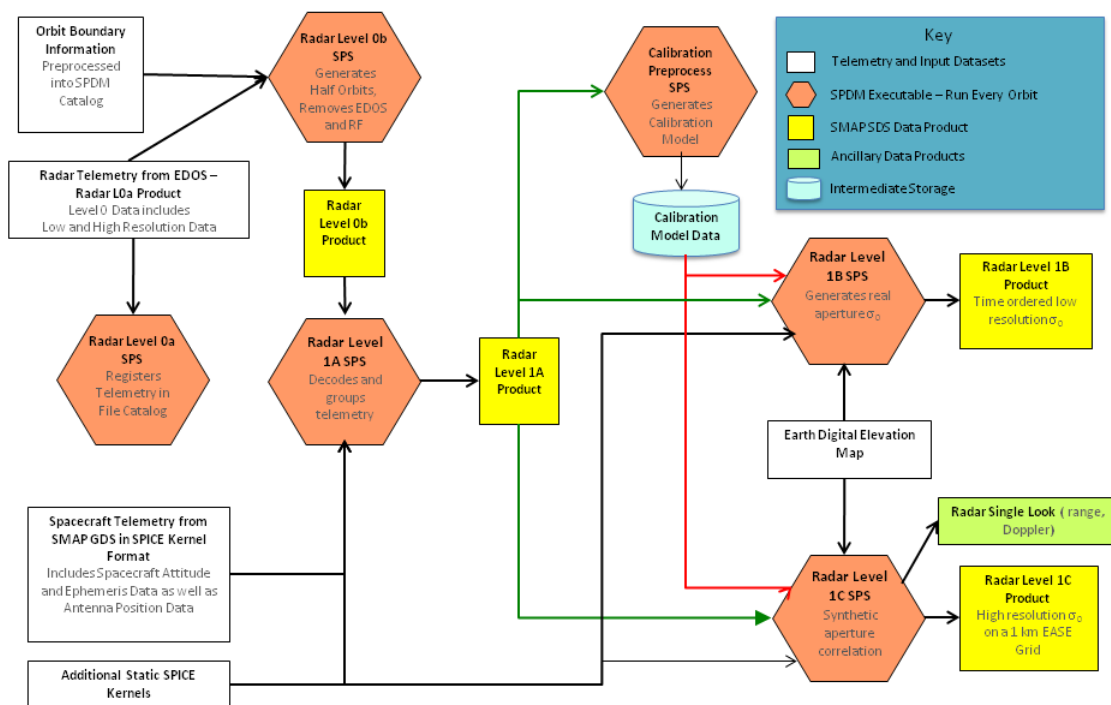


Figure 2: Flow of data in the SMAP level 0 and level 1 processors. The L0a processor assigns time meta-data to the incoming radar telemetry files. The L0b processor performs splitting and merging of the telemetry data to make half-orbit granules that contain all radar data that contributes to a given ascending or descending half-orbit granule. The L1A processor decodes and unpacks the radar telemetry, producing a L1A product in HDF5 format. The L1B processor applies calibration and geolocation to the low-resolution radar data produced by the radar hardware. The L1C processor does SAR correlation processing as well as applying calibration and geolocation to the high-resolution radar data. The calibration processor extracts special calibration data and updates calibration models used by the L1B and L1C processors. Additional ephemeris, attitude, and time information needed by all processors is supplied in the form of SPICE binary and text kernel files.

body ephemeris data and other cartographic data, I-kernels which contain instrument data, C-kernels which contain pointing or attitude data, and E-kernels which contain special event information. Collectively these kernel files are called SPICE files using the first letter of each type in the acronym. SPICE files follow format standards used by many JPL planetary missions and include a software library to access and manipulate them. More detailed information about NAIF and SPICE is available at [naif.jpl.nasa.gov](http://naif.jpl.nasa.gov). The topographic data file (DEM) will be constructed for use by all the SMAP level processors using primarily SRTM data plus three additional sources of survey data from the USGS and Canada's GeoBase for high latitude coverage. All of these data sets are interpolated to 1 arcsec resolution (30 m) on the Earth's surface. The zero-reference is the WGS84 ellipsoid. Further details on the DEM can be found in [4]. The L1A,B,C processors will all ingest the SPICE files and the DEM file to perform geometry calculations. Additional interpolation inside these processors is expected to improve performance.

#### **4.1.2 Instrument Data**

Instrument data consist of all the radar and spacecraft telemetry data needed to perform the SAR correlation (eg., PRI) and to calibrate the data. Most of these data are supplied by telemetry fields in the raw data file, and some others that are measured before launch will be held in a radar processing configuration file.

#### **4.1.3 Processing Parameters**

Processing parameters will be supplied in the radar processing configuration file. These include parameters like the amount of Doppler bandwidth to process that are entirely at the discretion of ground processing and are chosen to optimize the quality of the final  $\sigma_0$  measurements.

### **4.2 Output Data**

The interface with higher level processing is via the L1B and L1C product specifications which are described at a high level in this subsection. Full details are in the L1B and L1C product specification documents. Like the L1A product, the L1B and L1C products will be stored as HDF files and submitted for archival storage.

#### **4.2.1 L1B Product Description**

The output L1B file in HDF format contains 4 main sections of data. The first is a meta-data block which contains information about the entire file. Meta-data are

divided into two groups, a general group present in all SMAP data products (including higher levels), and a product specific group that contains more specialized fields appropriate to the corresponding product. The general fields include input and output file names, types, and versions, time ranges of the contained data, generating software names, versions, dates of modification, and producer description information. The product specific group for L1B includes bounding coordinates on the Earth for contained data, orbital parameters and times, output projection used, antenna rotation rate, product resolution, algorithm version, the DEM used, and thresholds applied during processing. Following the meta-data is the spacecraft data group, which records basic geometric fields once per conical scan. Included are the spacecraft position and attitude, and the nadir track position on the surface. Following the spacecraft data group is the  $\sigma_0$  data group, which consists of vectors of data organized in time-order. The primary field is the radar normalized backscattering cross-section ( $\sigma_0$ ) with one value per 48-PRI low-resolution interval. 1-D arrays with shapes of one value per low-resolution interval are called  $\sigma_0$  arrays. Included are vectors of data providing,

- Geographic coordinates
- Equal Area Scalable Earth (EASE) Grid coordinates
- Topographic data for the beam center point
- Geometric look vector data (eg., azimuth and incidence angles, range)
- Surface type flag
- Number of looks
- Data quality flags
- Normalized radar cross-section (NRCS,  $\sigma_0$ ) for all channels
- NRCS standard deviations for all channels
- Calibration factors used
- signal to noise ratio (SNR)
- spatial resolution

Because the vectors are organized in time-order, the spatial locations follow the scanning motion of the antenna, and the orbital motion of the spacecraft. These measurements are real-aperture results which apply to the full beam footprint on the surface (about 40 km across). The EASE Grid, discussed further in the next

section, is a set of standard projections used by many Earth Science Missions. Following the  $\sigma_0$  data group, is another set of 2-D arrays called the  $\sigma_0$  slice data group. These arrays divide the beam footprint into 9-14 range slices with sizes of about 6 km by 40 km. The same fields are present here as in the  $\sigma_0$  data group, but with higher range resolution. The range binning is actually done by the instrument before downlink to reduce data volume. These 2-D arrays called  $\sigma_0$  slice arrays will have a second dimension size determined by the L1A processor to accommodate the data take.

#### **4.2.2 L1C Product Description and Swath Grid**

The output L1C product in HDF format is spatially organized (unlike the time-ordered L1B product) using a 2-D swath grid. A special coordinate system developed at JPL [5] called SCH coordinates defines the swath grid used to project the output data. SCH coordinates are a spherical coordinate system that best approximates the WGS84 ellipsoid in the along track direction. This coordinate system is readily referenced to conventional geodetic coordinates (latitude and longitude) and these coordinates are also supplied in the output swath format. The transformation between SCH coordinates and WGS84 coordinates is completely specified by three parameters called peg parameters. Peg parameters consist of the latitude and longitude of the location where the approximating sphere is tangent to the ellipsoid, along with the ground track heading at that point which is used to compute the radius of the approximating sphere. As the distance along track from the peg point increases, the equator of the approximating sphere will start to deviate from the actual ground track thus requiring periodic updating of the peg point. The spacing of peg point updates is still TBD, but it will be selected to keep the grid cell location errors smaller than 0.5 km. The peg point updates will then be transparent to L1C users.

Level 2 and higher SMAP products are also spatially organized, but they will use EASE Grid projections instead of a swath oriented projection. There are three EASE Grid projections all of which will be used by SMAP data products. The cylindrical projection will be used for the bulk of the data. Two polar projections (one North, one South) will be used for high latitude data. To aid in translating data between the the swath grid and the EASE Grids, the L1C product will include the index coordinates of the cylindrical and one of the polar EASE Grids along with the WGS84 latitude and longitude for each swath grid square. All of these will apply to the center point of each swath grid square. The swath grid will have approximately 1 km posting, however it should be noted that all performance requirements listed in tables 1 and 3 are specified for the corresponding 3-km grid obtained by averaging down the 1-km grid. The L1C product uses the swath grid rather than one of the EASE Grids because the swath grid is more space efficient (fewer empty array

positions in a half-orbit), and suffers from much less distortion. Furthermore, many important performance characteristics of the radar data such as the number of looks, the effective resolution, and the random error are functions of cross-track position but not of along-track position. Using a swath grid will then make validation of the data an easier task.

The L1C product contains three sections of data. The first is the same meta-data present in the L1B file. The second is the spacecraft data group which contains time-ordered geometry data (spacecraft position, velocity, and attitude) at the times when the spacecraft nadir point crosses the midpoints of each swath row. The third is the  $\sigma_0$  data group organized as 2-D swath grid arrays. The primary field again is the  $\sigma_0$  field. The L1C SAR processing algorithms will geolocate  $\sigma_0$  results with respect to the 3-D ellipsoidal surface of the Earth as defined by the WGS84 Earth model. These data are then projected onto the 2-D swath grid. The same basic data fields listed earlier for the L1B file are also present in L1C files, but they will be 2-D spatially organized arrays rather than 1-D time-ordered vectors.

### 4.3 Bit Flags in L1B and L1C products

Numerous bit flags are included in the L1B and L1C products to convey useful information about the associated data fields. As a general rule, bit flags are defined so that the value of one (true) indicates the presence of some adverse condition such as an error above a requirement threshold, or the absence of data needed to compute a result. Conversely, the value of zero (false) means the associated data are “good”. Related bit flags are grouped together in 16-bit integers with array dimensions matching the associated data. The L1B product has time-ordered bit flag fields with shapes corresponding to both  $\sigma_0$  arrays and  $\sigma_0$  slice arrays. The L1C product has spatially ordered bit flag fields with shapes corresponding to the swath grid. The 16-bit integer fields containing bit flags are summarized in table 4 for the L1B product, and in table 5 for the L1C product. The individual bit flags are then described in tables 6 - 11. Table 8 represents eight tables; four for whole footprint flags (HH,VV,VH,HV), and four for range slice flags (HH,VV,VH,HV). The range slice flag fields are 2-D with the 2nd dimension indexing the specific range slice. Table 11 represents three tables for the three polarization channels present in high-res data. These three channels are the two co-pol channels (HH,VV) and one of the cross-pol channels indicated by  $XY \in \{HV,VH\}$ . The specific cross-link channel used is selected by an uplinked command to the radar.

Table 4: L1B Bit Flag Fields

Field Name	Shape	Description
antenna_scan_qual_flag	antenna scan array	Flag relevant to spacecraft attitude
sigma0_mode_flag	$\sigma_0$ array	Flags describing special features of each $\sigma_0$ measurement
sigma0_qual_flag_hh	$\sigma_0$ array	Flags indicating quality issues with $\sigma_{0hh}$ full footprint measurements
sigma0_qual_flag_vv	$\sigma_0$ array	Flags indicating quality issues with $\sigma_{0vv}$ full footprint measurements
sigma0_qual_flag_hv	$\sigma_0$ array	Flags indicating quality issues with $\sigma_{0hv}$ full footprint measurements
sigma0_qual_flag_vh	$\sigma_0$ array	Flags indicating quality issues with $\sigma_{0vh}$ full footprint measurements
slice_qual_flag_hh	$\sigma_0$ slice array	Flags indicating quality issues with $\sigma_{0hh}$ range slice measurements
slice_qual_flag_vv	$\sigma_0$ slice array	Flags indicating quality issues with $\sigma_{0vv}$ range slice measurements
slice_qual_flag_hv	$\sigma_0$ slice array	Flags indicating quality issues with $\sigma_{0hv}$ range slice measurements
slice_qual_flag_vh	$\sigma_0$ slice array	Flags indicating quality issues with $\sigma_{0vh}$ range slice measurements

Table 5: L1C Bit Flag Fields

Field Name	Shape	Description
along_track_qual_flag	along track array	Flag relevant to spacecraft attitude
cell_mode_flag	swath array	Flags describing special features of each $\sigma_0$ measurement
cell_sigma0_qual_flag_hh	swath array	Flags indicating quality issues with gridded 1 km $\sigma_{0hh}$ measurements
cell_sigma0_qual_flag_vv	swath array	Flags indicating quality issues with gridded 1 km $\sigma_{0vv}$ measurements
cell_sigma0_qual_flag_xy	swath array	Flags indicating quality issues with gridded 1 km $\sigma_{0xy}$ measurements

Table 6: L1B antenna scan quality bit flags

Bit Pos.	Flag Description	Value	Interpretation
0	attitude mode	0	Spacecraft in normal Earth viewing mode
		1	Spacecraft viewing cold space for radiometer calibration
1-15	Not used		Always clear

Table 7: L1B  $\sigma_0$  mode bit flags

Bit Pos.	Flag Description	Value	Interpretation
0	Fore/Aft	0	$\sigma_0$ measurement center is forward of the spacecraft
		1	$\sigma_0$ measurement center is aft of the spacecraft
1	water	0	Water fraction of grid cell below metadata threshold
		1	Water fraction of grid cell exceeds metadata threshold
2-15	Not used		Always clear

Table 8: L1B  $\{\sigma_{0,xx}\}$ \_qual\_flag\_xx ( $xx \in \{hh,vv,hv,vh\}$ )

Bit Pos.	Flag Description	Value	Interpretation
0	quality	0	$\sigma_{0,xx}$ meets error requirements
		1	$\sigma_{0,xx}$ does not meet error requirements
1	range	0	$\sigma_{0,xx}$ falls within expected range
		1	$\sigma_{0,xx}$ falls outside of expected range
2	RFI level	0	$\sigma_{0,xx}$ had insignificant RFI power detected
		1	$\sigma_{0,xx}$ had significant RFI power detected and correction was attempted
3	RFI correction	0	$\sigma_{0,xx}$ corrected for detected RFI
		1	$\sigma_{0,xx}$ bad due to uncorrectable RFI
4	bit correction	0	No bit errors detected in $\sigma_{0,xx}$ data
		1	Bit errors detected in $\sigma_{0,xx}$ data
5	nadir gap	0	No data from the nadir gap area were used by $\sigma_{0,xx}$
		1	Data from the nadir gap area were used by $\sigma_{0,xx}$
6	nadir gap	0	No data from the nadir gap area were used by $\sigma_{0,xx}$
		1	Data from the nadir gap area were used by $\sigma_{0,xx}$
7-15	Not used		Always clear

Table 9: L1C antenna scan quality bit flags

Bit Pos.	Flag Description	Value	Interpretation
0	attitude mode	0	Spacecraft in normal Earth viewing mode
		1	Spacecraft viewing cold space for radiometer calibration
1-15	Not used		Always clear

Table 10: L1C cell mode bit flags

Bit Pos.	Flag Description	Value	Interpretation
0	nadir gap	0	No data from the nadir gap area were used by $\sigma_0$
		1	Data from the nadir gap area were used by $\sigma_0$
1	nadir gap	0	No data from the nadir gap area were used by $\sigma_0$
		1	Data from the nadir gap area were used by $\sigma_0$
2	water	0	Water fraction of grid cell below metadata threshold
		1	Water fraction of grid cell exceeds metadata threshold
3	resolution	0	Radar resolution is better than 9 km
		1	Radar resolution is worse than 9 km
4-15	Not used		Always clear (Bits 4-7 reserved for L1. Bits 8-15 reserved for L2)

## 5 Data Characteristics and Radar Performance

SMAP radar data have some unique characteristics compared to other radar missions. Some of the unique character of the SMAP radar data comes from doing SAR imaging on a conically scanned system. All forms of SAR imaging effectively divide the radar echo energy into range bins and doppler bins. The sorting process is effected by correlation processing algorithms described in the next sections. Even without knowing the algorithm details, we can explore some of the expected characteristics of the data. A more detailed discussion of the performance and design issues for a conically scanned radar using SAR techniques is presented in [6].

### 5.1 Radar Resolution

Figure 3 shows the range/doppler structure underneath the conically scanning SMAP radar.  $V_g$  shows the spacecraft motion projected on the surface, and CTD is the orthogonal cross track distance direction. Curves of constant range appear approximately as circles formed by intersecting a cone with the Earth's surface. The cone is centered on the nadir vector from the spacecraft with the spacecraft at the apex. The ellisoidal shape of the Earth will distort true iso-range curves into slightly elliptical shape. These iso-range lines are shown as the thin line circles in Fig. 3. Doppler shift is proportional to the projection of the spacecraft relative velocity along the look direction, so lines of constant doppler are formed by intersecting a cone about

Table 11: L1C cell\_sigma0\_qual\_flag\_xx ( $xx \in \{hh,vv,xy\}$ )

Bit Pos.	Flag Description	Value	Interpretation
0	fwd quality	0	Forward looking $\sigma_{0xx}$ meets error requirements
		1	Forward looking $\sigma_{0xx}$ does not meet error requirements
1	aft quality	0	Aft looking $\sigma_{0xx}$ meets error requirements
		1	Aft looking $\sigma_{0xx}$ does not meet error requirements
2	fwd range	0	Forward looking $\sigma_{0xx}$ falls within expected range
		1	Forward looking $\sigma_{0xx}$ falls outside of expected range
3	aft range	0	Aft looking $\sigma_{0xx}$ falls within expected range
		1	Aft looking $\sigma_{0xx}$ falls outside of expected range
4	fwd RFI level	0	Forward looking $\sigma_{0xx}$ had insignificant RFI power detected
		1	Forward looking $\sigma_{0xx}$ had significant RFI power detected and correction was attempted
5	fwd RFI correction	0	Forward looking $\sigma_{0xx}$ corrected for detected RFI
		1	$\sigma_{0xx}$ bad due to uncorrectable RFI
6	aft RFI level	0	Aft looking $\sigma_{0xx}$ had insignificant RFI power detected
		1	Aft looking $\sigma_{0xx}$ had significant RFI power detected and correction was attempted
7	aft RFI correction	0	Aft looking $\sigma_{0xx}$ corrected for detected RFI
		1	Aft looking $\sigma_{0xx}$ bad due to uncorrectable RFI
8-15	Not used		Always clear (Bits 8-11 reserved for L1. Bits 12-15 reserved for L2)

the spacecraft velocity vector with the Earth's surface. These iso-doppler curves are shown on the figure as straight to hyperbolic thin lines. The SMAP conical scan maintains an incidence angle of 40 degrees, and the actively imaged area is thus an annulus covered by the beam footprint. The swath is filled in by repeated conical scans which slightly overlap along the nadir track as shown in Fig 4.

SAR processing yields single look resolution cells bounded by iso-range and iso-doppler contours within the beam footprint. For conically scanned systems, it is convenient to think in terms of range or elevation resolution directed radially away from the sub-spacecraft nadir point and azimuth resolution directed along the scan motion of the beam footprint. Assuming a spherical Earth, projected range resolution and azimuth resolution are given by,

$$\delta R_g = \frac{c}{2B_r \sin \theta_i}, \quad (1)$$

$$\delta x = \frac{\lambda R}{2\tau_d v} f(\theta_{az}), \quad (2)$$

where  $\delta R_g$  is the projected range resolution on the surface,  $c$  is the speed of light,  $B_r$  is the transmitted chirp bandwidth,  $\theta_i$  is the incidence angle,  $\delta x$  is the azimuth resolution on the surface,  $\lambda$  is the transmitted wavelength,  $R$  is the slant range,  $\tau_d$  is the beam dwell time or synthetic aperture time,  $v$  is the magnitude of the spacecraft velocity relative to the target body, and  $f(\theta_{az})$  is the squint elongation varying as a function of the scan angle position  $\theta_{az}$  as described in [6]. Projected range resolution is constant around the scan at 230 m. Azimuth resolution degrades as the squint angle increases due to varying doppler spread and elongation of the resolution cells as iso-range and iso-doppler lines become more parallel to each other. Figure 5 shows the variation of single look resolution as a function of cross track distance.

Although Fig. 5 shows highly variable azimuth resolution across the swath, and fairly fine range resolution, the L1C product will not provide access to the single look resolution cells. Instead, multiple resolution cells are averaged together using area weighting into 1 km grid cells in the L1C product file. Two kinds of multi-looking occur in this step. First, resolution will be degraded to the 1 km posting of the L1C swath grid. This tradeoff is accepted in return for reduced statistical variation of the measurements and reduced data volume in the product. Second, multiple scans that cover the same 1 km cell will have their measurements averaged together for further reduction of statistical variation. However, forward and aft directed look directions will be kept separate so that azimuthal asymmetry of the target scene can still be observed. The resolution of the L1C product is then slightly less than 1 km with slight variation crosstrack due to the area weighting of resolution cells into the 1 km cells. Near the outer edge of the swath, resolution cells that stick outside of the 1 km cell by half their size (200 m) will broaden resolution by 20%. Near the inner edge of the usable swath (150 km crosstrack) resolution cells are elongated and can

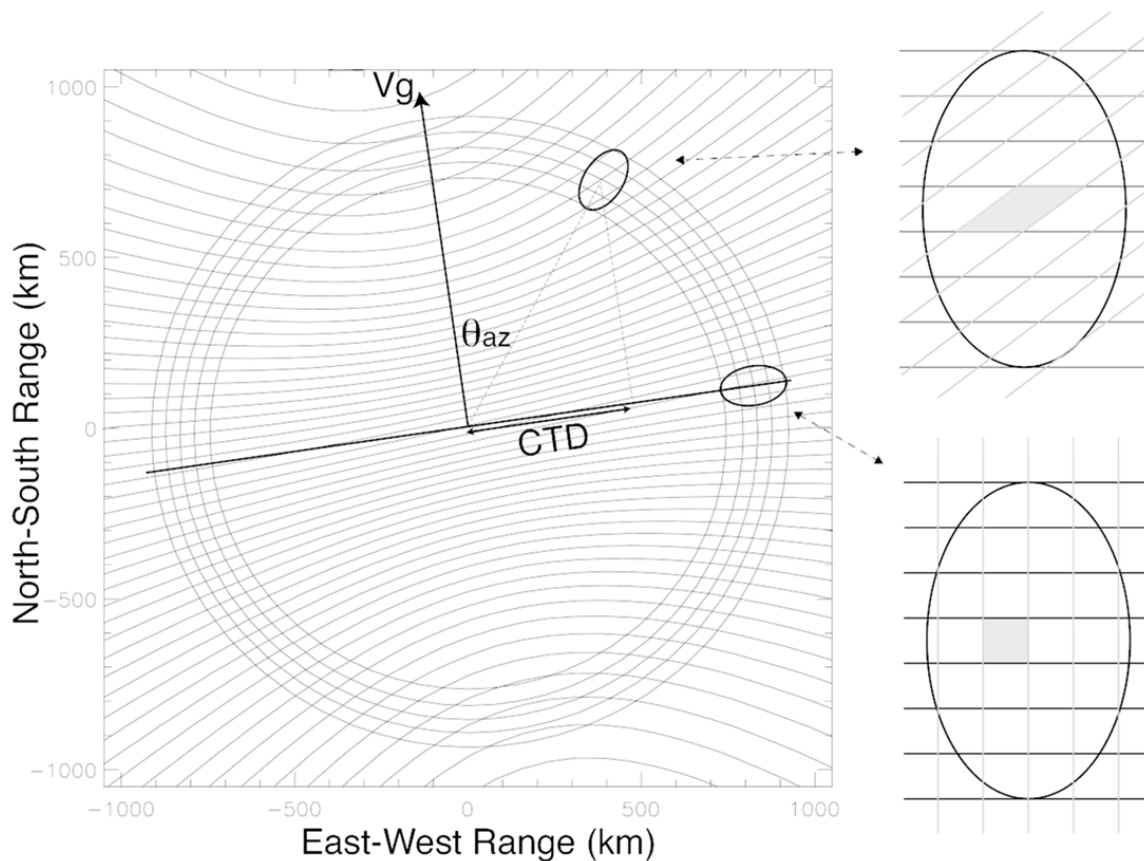


Figure 3: Iso-range/Iso-doppler structure and relationship to the conically scanned beam footprint. SAR processing produces resolution cells bounded by iso-range and iso-doppler lines with spacing determined by the chirp bandwidth and the beam dwell time over a particular point. Resolution cells are relatively square rectangles in the side-looking position, but become elongated parallelograms in highly squinted positions. In the nadir region, iso-range and iso-doppler lines are approximately parallel, and only range slicing can be done. Azimuth resolution degrades to the beamwidth. (See fig. 2 in [6])

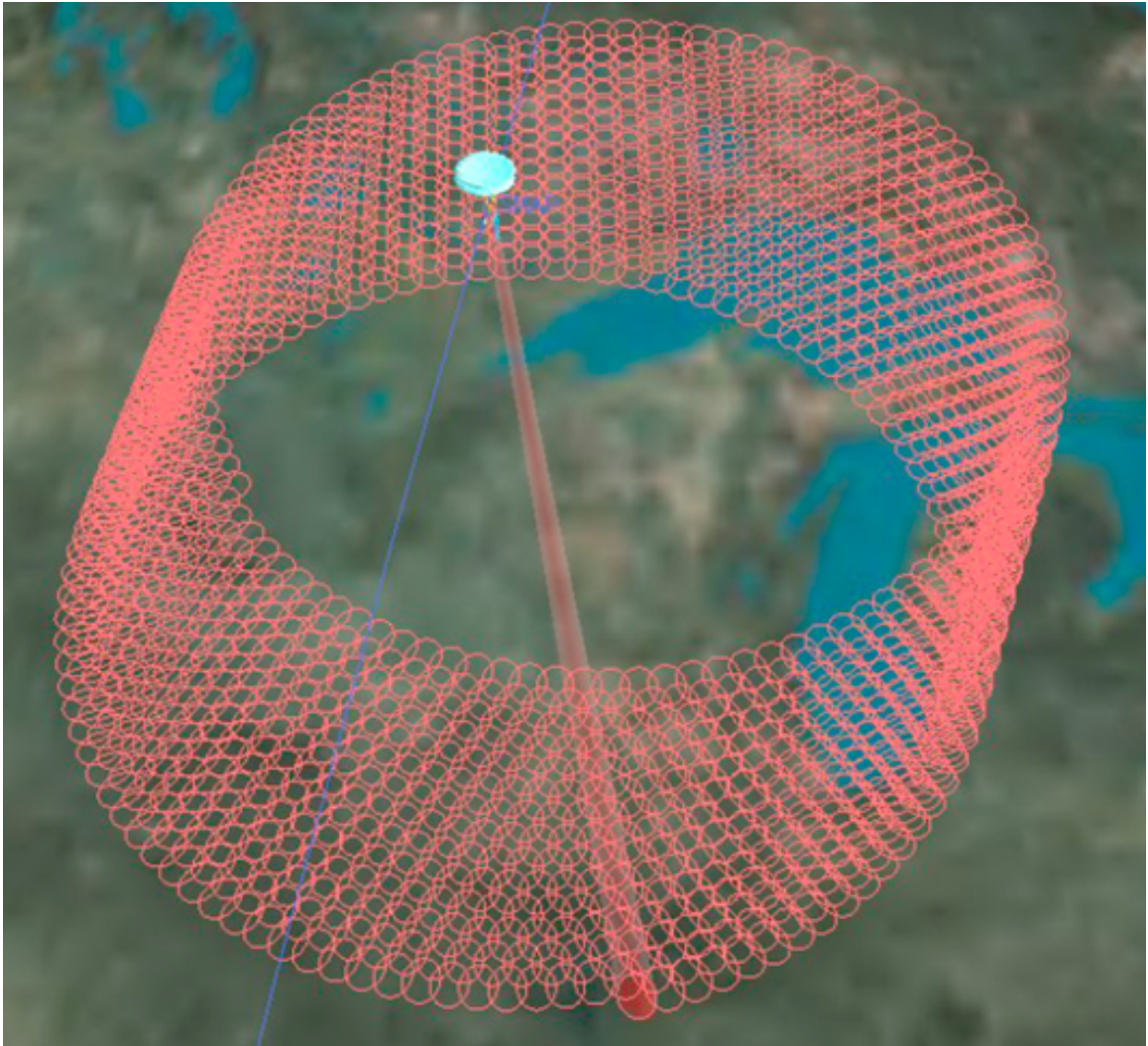


Figure 4: Overlapping conical scans building up as the spacecraft flies a descending orbit track. The scan rotation rate of 14.6 rpm was selected to provide some overlap along the nadir track thus filling in the 1000 km wide swath with radar measurements.

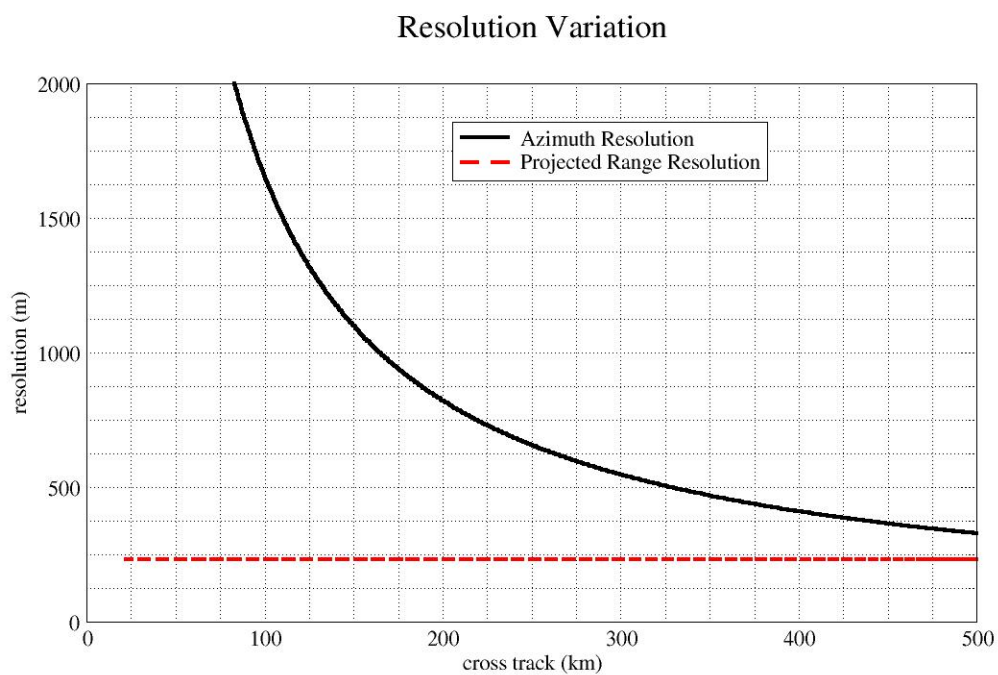


Figure 5: Resolution variation of single look resolution cells as a function of cross track distance. Side looking geometry which occurs at the edges of the swath (500 km cross track) gives the best azimuth resolution because iso-range and iso-doppler contours are orthogonal here. Lower cross track distances are obtained at higher squint angles as the conical scan proceeds and azimuth resolution degrades.

hang out by 500 m thus broadening resolution by 50%. In level 2 processing, the 1 km radar data will be further averaged down to at least 3 km posting which is the resolution that requirements are specified for.

## 6 Point Target Response and Time Range Definitions

Before getting into the details of the processing algorithms, we need to understand four key time ranges that come out of the way SMAP radar data are collected. This section, will examine the radar point target response which is of central importance in SAR processing, and define the associated time ranges.

The radar operates by continuously transmitting pulses and recording echoes during receive windows interleaved between the transmit times. High resolution data consist of the basebanded complex (I,Q) data samples spaced at the sample rate (1.25 MHz) from each consecutive receive window spaced at the pulse repetition interval (PRI). Round trip travel times at light speed from the spacecraft to the Earth's surface will lead to about 18 pulses in flight. Thus, the received echo from one particular transmit event would be recorded 18 PRI later in the received data. The precise position of the echo in the receive window depends on the range to the surface which will include some variability due to topography. The receive windows are long enough to accomodate most of this topographic variability, although there may be some data loss in very mountainous areas such as the Himalayas. If a single idealized point target on the surface is considered with no reflectivity anywhere else, then the echo recorded is called a point target response, or an impulse response. The point target response is a time and frequency shifted replica of the transmitted waveform. The next section describes the transmitted waveform.

### 6.1 Radar RF Signal Generation

Figure 6 shows a schematic view of the SMAP radar RF front end as currently designed. This figure is still a preliminary version and the final design will likely differ in the details. The following frequency and time definitions consistent with Fig. 6 are established:

$$f_{stalo} = 10 \text{ MHz} \quad (3)$$

$$f_{ctu} = f_{stalo}/8 = 1.25 \text{ MHz} \quad (4)$$

$$f_{cg(n,h,v)} = m_{cg(n,h,v)} f_{ctu} \quad (5)$$

$$f_u = m_u f_{ctu} \quad (6)$$

$$f_d = m_d f_{ctu} \quad (7)$$

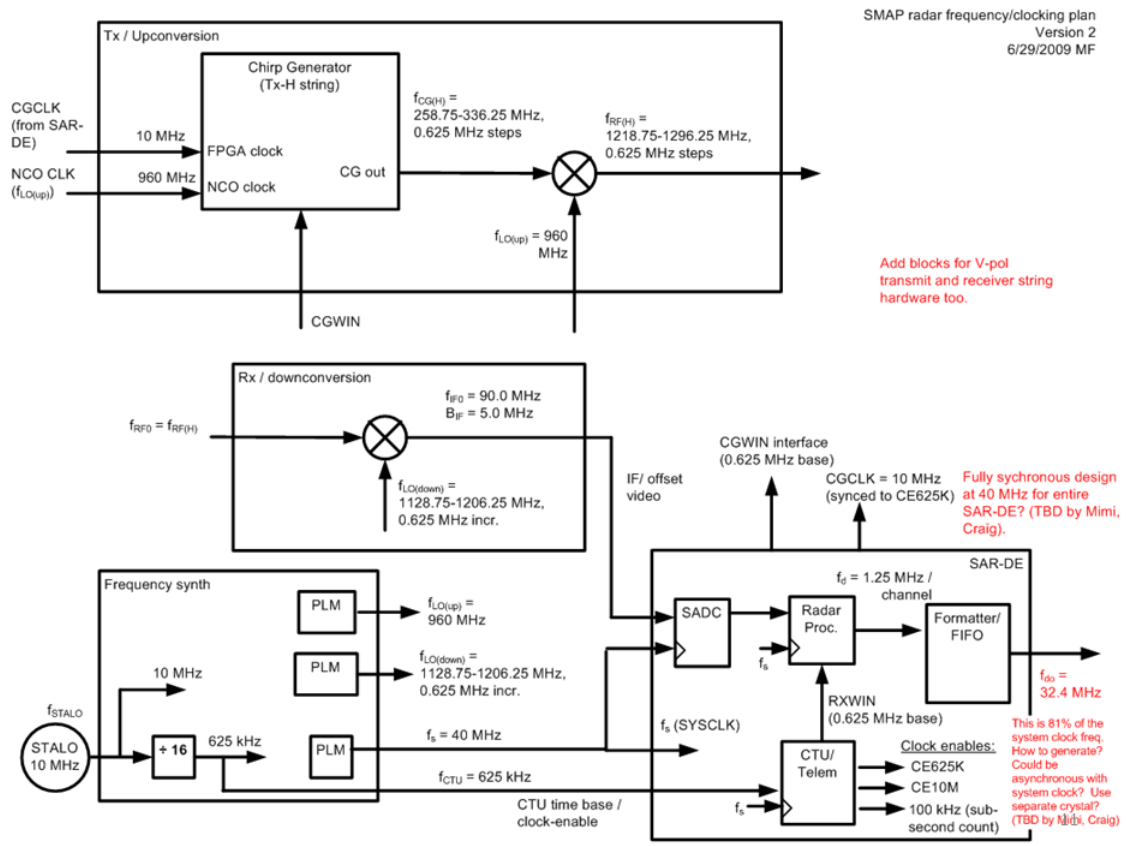


Figure 6: Chirp generation and RF mixup/down design for the SMAP radar. This figure still shows the old 625 KHz CTU frequency. Needs to be updated with new design based on 1.25 MHz CTU frequency when available.

$$\tau_{pri} = \frac{n_1}{f_{stalo}} \quad (8)$$

$$\tau_p = \frac{150}{f_{stalo}} \quad (9)$$

$f_{stalo}$  is the stable local oscillator (STALO) from which all timing signals are derived.  $f_{ctu}$  is the base frequency used in the control and timing unit and it is derived by dividing  $f_{stalo}$  by 8.  $f_{cg(n,h,v)}$  is the center frequency of the output step chirp produced by the chirp generator.  $f_{cgn}$  gives the noise channel center frequency as an integer multiple of  $f_{ctu}$  with  $m_{cgn} \in [207, 269]$ . Note that the end values are included in  $m_{cgn}$  giving 63 separate values. No chirp is actually produced for the noise channel. Instead, an H-pol chirp is produced with a center frequency 1.5 MHz higher than the noise channel center frequency, and a V-pol chirp is produced 1.5 MHz lower. The chirp generator is not limited to integer multiples of  $f_{ctu}$ , but rather synthesizes a waveform with a fundamental step size given by the supplied 960 MHz clock. Since the channel spacing of 1.5 MHz is not an integer multiple of  $f_{ctu}$ , the effective multipliers for the H-pol channel and the V-pol channel are not integers:  $f_{cgh} = (m_{cgn} + \frac{6}{5})f_{ctu}$  and  $f_{cgv} = (m_{cgn} - \frac{6}{5})f_{ctu}$ .

The radar transmits a step chirp waveform with 1 MHz bandwidth that can be approximated as a linear FM chirp with a frequency chirp rate  $K_1$  given by

$$K_1 = \frac{1 \text{ MHz}}{\tau_p} \quad (10)$$

where  $\tau_p = 15 \mu\text{s}$  is the nominal pulse length. The system is designed to tune the transmitted 1 MHz chirp across the 80 MHz allocated band in 1.25 MHz steps to avoid RFI as a function of scan and orbit position. Transmit tuning is implemented with a digital chirp generator that synthesizes H-pol chirps in the range 260.25 MHz - 337.75 MHz with 1.25 MHz steps (63 frequency choices in total). The corresponding V-pol chirps are offset 3 MHz lower in frequency, leaving a 1 MHz noise only channel inbetween the H-pol and V-pol channels.

The PRI is an integer multiple ( $n_1$ ) of the STALO period. For SMAP,  $n_1 \in [2800, 3776]$  gives a PRI range of 280  $\mu\text{s}$  to 377.6  $\mu\text{s}$  spaced at 0.1  $\mu\text{s}$  with 977 separate values that can be commanded. The chirp generator produces a pulse stream  $s_{cg}$  with a spacing of  $\tau_{pri}$ , and with a sine starting phase of 0 using the sine start option for each pulse. Thus,

$$u_p(t) = \begin{cases} 1 & \text{for } -\frac{\tau_p}{2} < t < \frac{\tau_p}{2} \\ 0 & \text{otherwise} \end{cases} \quad (11)$$

$$s_{cg}(t, i) = s_{cg}(t - i\tau_{pri}) = u_p(t - i\tau_{pri}) \cos(2\pi f_{cg}(t - i\tau_{pri}) + \pi K_1(t - i\tau_{pri})^2 + \phi_{cg}), \quad (12)$$

where  $t$  is time starting from an arbitrary zero point,  $\phi_{cg}$  is the selected starting phase of the waveform (90 deg for the sine option) and  $i$  is the integer pulse position given by

$$i = \text{round}\left(\frac{t}{\tau_{pri}}\right) \quad (13)$$

and

$$\text{round}(x) = \text{int}(x + 0.5 \text{sign}(x)) \quad (14)$$

where  $\text{int}$  takes the integer part of a number, discarding any fractional part, and  $\text{sign}$  is  $+1$  for positive numbers and  $-1$  for negative numbers. A pulse train of  $N_p$  pulses can then be written as

$$s_{cg}(t) = \sum_{i=0}^{N_p} s_{cg}(t, i) \quad (15)$$

By separating out the pulse position, the time  $t$  is effectively restricted to the range  $[-\tau_{pri}/2, \tau_{pri}/2]$ , and both  $i$  and  $t$  are needed to fully specify a general time. In these equations, the subscript  $(n, h, v)$  is implicit where appropriate (eg.,  $s_{cg}$ ,  $f_{cg}$ ) except where a distinction between the three channels needs to be made.

The intermediate frequency chirp signal  $s_{cg}$  is mixed up with a continuous mixup signal given by

$$s_u(t) = \cos(2\pi f_u t + \phi_u) \quad (16)$$

where  $\phi_u$  is an arbitrary starting phase for the mixup signal which is a continuous running sinusoid. The mixup frequency  $f_u = m_u f_{ctu}$  is selected to be an integer multiple of both  $f_{stalo}$  and  $f_{ctu}$  to maintain a synchronous system. The current choice is  $m_u = 768 = 96 \cdot 8$ . The mixup process means multiplying the chirp signal with the mixup signal and filtering out the upper sideband which yields the desired L-band RF signal for transmission. Using the following trigonometric identity,

$$\cos a \cos b = \frac{1}{2}(\cos(a - b) + \cos(a + b)), \quad (17)$$

and renormalizing to unit magnitude gives,

$$s_{rf}(t, i) = u_p(t - i\tau_{pri}) \cos(2\pi(f_{cg} + f_u)t - 2\pi f_{cg}i\tau_{pri} + \pi K_1(t - i\tau_{pri})^2 + \phi_u + \phi_{cg}). \quad (18)$$

## 6.2 Basebanded Point Target Response

The received echo from a point target will be the same waveform delayed in time by the travel time to and from the point on the surface. If the range to the surface point is  $R(t)$ , then the travel delay is  $\Delta t = 2R(t)/c$ , where  $c$  is the speed of light,

and  $R(t)$  indicates that the range is a function of time because of spacecraft motion. By including the time dependence of  $R$ , the Doppler frequency shift of the echo waveform due to the motion of the spacecraft relative to the surface point is automatically included. The received waveform ( $V_{rf}$  in volts) is then given by

$$\begin{aligned} V_{rf}(t) &= A s_{rf}(t - 2R(t)/c) \\ &= A u_p(t - 2R(t)/c - i\tau_{pri}) \cos(2\pi f_{cg}(t - 2R(t)/c - i\tau_{pri}) + 2\pi f_u(t - 2R(t)/c) \\ &\quad + \pi K_1(t - 2R(t)/c - i\tau_{pri})^2) + \phi_u + \phi_{cg} \end{aligned} \quad (19)$$

The received RF signal is first mixed down with another continuous running sinusoid at frequency  $f_d = m_d f_{ctu}$ .

$$s_d(t) = \cos(2\pi f_d t + \phi_d) \quad (20)$$

where  $\phi_d$  is an arbitrary starting phase for the mixdown signal. To deliver an intermediate frequency of 90 MHz regardless of the transmit tuning, the value of  $m_d$  is chosen from the range [903, 965] synchronized by index with the values of  $m_{cg}$  used by  $f_{cg}$ . The result of multiplying  $s_{rf}$  and  $s_d$  and taking the lower sideband is

$$\begin{aligned} V_{if}(t, i) &= A u_p(t - 2R(t)/c - i\tau_{pri}) \cos(2\pi f_{cg}(t - 2R(t)/c - i\tau_{pri}) + 2\pi f_u(t - 2R(t)/c) - 2\pi f_d t \\ &\quad + \pi K_1(t - 2R(t)/c - i\tau_{pri})^2) + \phi_u - \phi_d + \phi_{cg} \end{aligned} \quad (21)$$

As shown in Fig. 6, the IF signal centered at 90 MHz is sampled at 40 MHz which undersamples the signal. The IF signal is 5 MHz wide and includes the H-pol, noise channel, and V-pol band passes spaced 1.5 MHz apart. Aliasing will cause the IF signal to show up in the 20 MHz bandwidth of the ADC samples centered at 11.5 MHz for H-pol data, 10.0 MHz for noise only data, and 8.5 MHz for V-pol data.

The final filtering and IQ demodulation for each of the three channels is performed digitally in the radar FPGA. The filtering is done by high order FIR digital filters that offer a sharp cutoff and a bandwidth of about 1.1 MHz for each channel. The demodulation and aliasing can be modeled as another mixdown with the mixdown frequency chosen to match each channel IF center frequency. Here it is assumed that the demodulation mixdown starts from zero phase for each pulse just like the chirp generator

$$s_{demod}(t, i) = s_{demod}(t - i\tau_{pri}) = \cos(2\pi(f_{cg} + f_u - f_d)(t - i\tau_{pri})) \quad (22)$$

Multiplying  $s_{if}$  by  $s_{demod}$  and taking the lower sideband gives the final complex basebanded point target response

$$\begin{aligned} V_{bbpt}(t, i) &= A u_p(t - 2R(t)/c - i\tau_{pri}) \exp(j2\pi(f_u - f_d)i\tau_{pri} - j4\pi(f_{cg} + f_u)R(t)/c \\ &\quad + j\pi K_1(t - 2R(t)/c - i\tau_{pri})^2) + j(\phi_u - \phi_d + \phi_{cg}) \end{aligned} \quad (23)$$

The complex exponential in Equation 23 gives both the I (real) and Q (imaginary) components. The first phase term  $(2\pi(f_u - f_d)i\tau_{pri})$  describes a pulse to pulse phase progression that occurs for certain choices of frequency and PRI. Correction of this effect is discussed in a later subsection. The second phase term  $(4\pi(f_{cg} + f_u)R(t)/c)$  is the Doppler phase term that SAR processing exploits to achieve azimuth compression. It describes the Doppler chirp that a given target will produce while it is in view of the antenna main lobe. The third phase term  $(\pi K_1(t - 2R(t)/c - i\tau_{pri})^2)$  is the quadratic phase from the linear FM chirp. This term provides range resolution and is removed during initial range compression processing. The final phase term  $\phi_u - \phi_d + \phi_{cg}$  is a fixed phase offset introduced by the mixup, mixdown stages, and the chirp generator. Fixed phase offsets have no effect on subsequent processing and can be ignored.

The amplitude of the received signal is attenuated according to the point radar equation (see eqn. 7.10 in [8]),

$$P_s = \frac{P_t G^2 \lambda^2 \sigma}{(4\pi)^3 R^4} \quad (24)$$

where  $P_s$  is the received signal power measured at the antenna port,  $P_t$  is the average radiated power during the transmit pulse,  $G$  is the one-way antenna power gain in the direction of the point target,  $\lambda$  is the RF wavelength corresponding to the chirp center frequency, and  $\sigma$  is the cross-section of the point target with units of area. The time dependence of  $R$  could be included here, but it is less critical to radiometric calibration than it is in the phase terms. Simply using the range at the center of the echo window should be sufficient. The amplitude of the digitized data is also increased by the gain of the receiver  $G_r$ , and multiplied by the conversion constant of the analog to digital converter  $C_{adc}$  which relates watts to counts. Thus,

$$A^2 = \frac{P_t G_r C_{adc} G^2 \lambda^2 \sigma}{(4\pi)^3 R^4} \quad (25)$$

The values of  $P_t$ ,  $G_r$ ,  $C_{adc}$ , and  $G$  will be measured during pre-launch testing. Tracking variations in these parameters is discussed in the Calibration section later in this document.

### 6.3 Forward and Backward Swath Row Time Range

Equation 23 gives the functional form of the point target response. Next, the time extent of point target responses in the data samples is defined. The longest and highest level of time ranges are the forward and backward swath row time ranges, and the shortest time range is the impulse response time. The forward swath row time range is the time extent during which point targets located in a given cross track

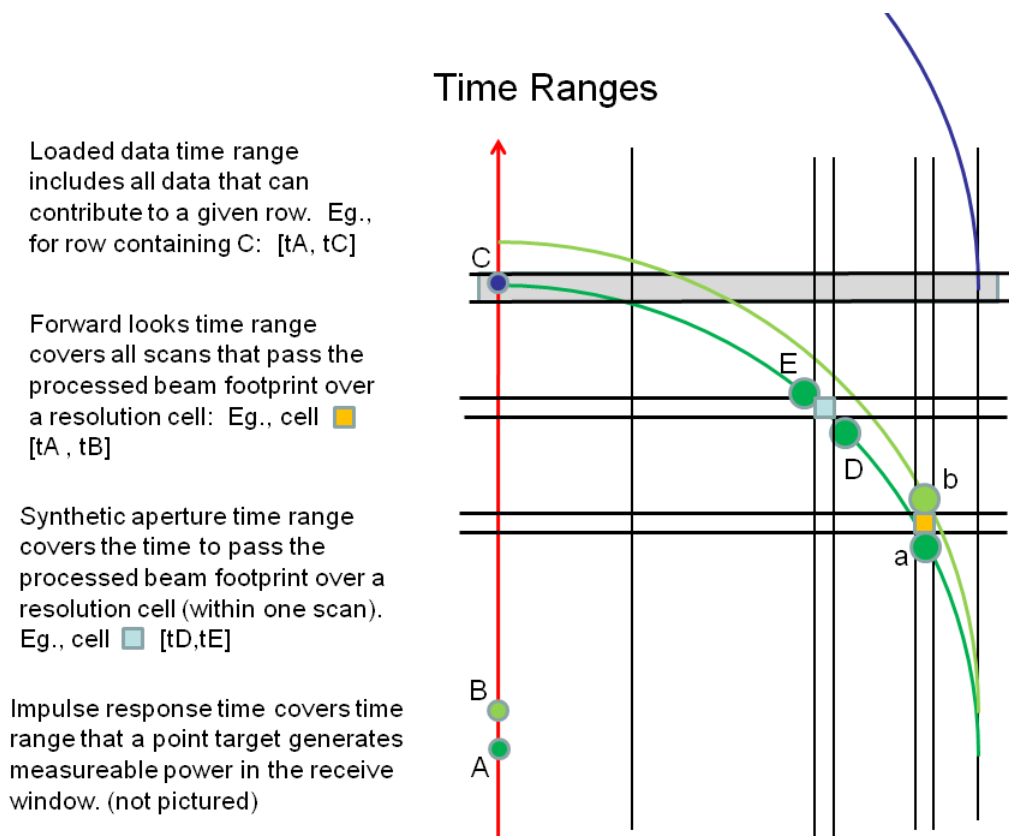


Figure 7: Schematic view of the nadir track, conical scans, and beam footprint positions that define the four key time ranges. The leftmost vertical line and arrow shows the motion of the sub-spacecraft point (nadir point) across the Earth's surface. The circular arcs show the motion of the beam boresight across the surface due to the conical scans. Portions of 3 conical scans are shown. The larger circular spots represent the beam footprint on the surface and illustrate the overlap of conical scans for a given 1 km grid square, and the time span of a synthetic aperture within one conical scan. The vertical extent of the figure shows the time range over which forward looks will accumulate in the shaded row. This determines the time range of data that needs to be loaded into memory for processing.

row of the swath grid will produce significant echo energy in the receive windows using the forward looking half of the scan. Figure 7 shows a schematic of the swath and conical scans to help visualize the time ranges. On this figure, the swath row time range for the grayed row containing point C on the left covers  $[t_A, t_C]$  where  $t_A$  is the time at which the spacecraft flies over nadir point A at which point the leftmost part of the row is scanned. Similarly,  $t_C$  is the time when the spacecraft flies over nadir point C at which point the far right side of the row is scanned. Intermediate cross track positions are scanned at times inbetween  $t_A$  and  $t_C$ . The swath row time range is important because the L1C processor will keep data loaded in memory sufficient to completely process a row of output. Once the processor moves beyond  $t_C$  in the data, there will be no further forward look contributions to the indicated row which can then be written to the output file. Beyond point  $t_C$ , the backward looks for the grayed row begin and carry forward in a mirror image of the forward looks.

#### **6.4 Forward and Backward Looks Time Ranges**

The forward (and backward) looks time ranges cover all the conical scans which contribute significant echo energy for a particular point target. In the side looking scenario where the beam footprint is directed 90 degrees away from the nadir track, a given point on the surface will be observed by up to a dozen consecutive scans both forward and backward looking. As the point is moved in closer to the nadir track, the repeated looks separate into a group of consecutive forward looks and consecutive backward looks. The number of looks diminishes to about 1 at the nadir track where there is a minimum of overlap between scans. A given point target will therefore produce a number of discrete segments of data. Each of these will be separately processed and averaged together. An example is shown on Fig. 7 for scans occurring between  $[t_A, t_B]$ .

#### **6.5 Synthetic Aperture Time**

The synthetic aperture time range covers all the pulse times within one scan for which a given point target is within the beam footprint and producing significant echo power. For the nominal SMAP mission parameters, 14.6 rpm rotation rate, pulse repetition rate around 311 us, there will be around 120 pulse repetition intervals or 38 ms within one synthetic aperture time. On Fig. 7, an example of synthetic aperture time range is shown between points D and E. The synthetic aperture time fundamentally sets and limits the Doppler and azimuth resolution that can be achieved. The limit comes from the extent of Doppler variation that is sampled while a particular target point is being observed. Since Doppler and Doppler spread within a beam footprint vary around the conical scan, azimuth resolution will vary

from about 400 m in the side looking case to about 1200 m when at the 150 km inner edge of the usable swath. Accuracy considerations discussed later may lead the processor to use a smaller synthetic aperture time which would result in reduced azimuth resolution and ultimately fewer independent looks and higher statistical noise. Each of the 120 consecutive receive windows covered by a particular point target will contain a point target response given by Equation 23. The amplitude of each response will be different primarily because the antenna pattern gain  $G$  will be different since each lies at a different angle within the beam footprint. This antenna gain variation needs to be included in calibration processing discussed later.

## 6.6 Impulse Response Time

Receive windows are much longer than the pulse width because they have to accommodate the range spread within the beam footprint and leave some extra room to cover attitude control errors. A single point target, however, produces an echo that is one pulse width long and positioned within the receive window according to its range at the time of transmission. This time range is called the impulse response time, or alternatively the range gate time. The collection of impulse response times for all 120 receive windows within the synthetic aperture time for a point target are the footprint of that point target within the data. These data are identified and processed into a single look backscatter result for that point target position by the SAR processing algorithms discussed in the next section.

# 7 L1C Processing Algorithms

Once on the ground, the high-resolution and low-resolution data are processed through a series of steps as shown in figs. 8 and 13. This section will focus on the L1C SAR algorithm and the following section summarizes the simpler L1B algorithm.

## 7.1 Image Formation Theoretical Background

SAR processing algorithms have been covered extensively in text books such as [12] and [15]. Here we summarize the basic theoretical background needed for SMAP L1 SAR processing using material adapted from Ch's 3 and 4 of [12]. Equations 23 and 25 describe the echo signal recorded in the data from a point target as a function of time. The point target sits at range  $R(t)$  at time  $t$ . Before defining an image formation algorithm, we need to further specify the relationships between position, range, and time. Let  $\vec{r}_{sc}(t, i)$  be the position vector of the spacecraft at time  $t$  and pulse index  $i$  in Earth body fixed coordinates. Let  $\vec{r}$  be an arbitrary point on

the Earth's surface also in Earth body fixed coordinates. The range to the specified point on the Earth's surface as a function of time is then,

$$R(t) = |\vec{r}_{sc}(t, i) - \vec{r}|, \quad (26)$$

and we can define the point target response as a function of the two position vectors,

$$V_{bbpt}(t, i) \equiv h(\vec{r}_{sc}(t, i) - \vec{r}) \quad (27)$$

where the symbol  $h$  is used by convention to represent an impulse response. In reality, the radar will observe a distributed scene that consists of many individual scattering centers (point targets). Assuming that the radar system is linear, we can sum the individual point target responses to get the total response,

$$V_{bb}(\vec{r}_{sc}(t, i)) = \int_{\text{visible surface}} h(\vec{r}_{sc}(t, i) - \vec{r}) \zeta(\vec{r}') dA, \quad (28)$$

where  $V_{bb}(\vec{r}_{sc}(t, i))$  is the basebanded complex signal due to the entire distributed scene when the spacecraft lies at position  $\vec{r}_{sc}$  at time  $t$  for pulse  $i$ ,  $h(\vec{r}_{sc}(t, i) - \vec{r})$  is the Green's function (impulse response, or point target response) evaluated at time  $t$  for pulse  $i$  with a point target (impulse) located on the surface at position  $\vec{r}$ , and  $\zeta(\vec{r}')$  is the complex Fresnel reflection coefficient of the surface element  $dA$ . The differential area  $dA$  is projected on the surface and the limit of integration indicates that all surface areas visible to the radar should be integrated over. In practice, the domain of integration is limited to surface area that can contribute significant energy to the integral, which usually means the projected area of the antenna pattern main lobe. Note that the integral is 2-D and the surface coordinates can be expressed as along track and cross track coordinates.

Equation 28 shows that the recorded signals are formed by convolving the surface scene (described by  $\zeta(\vec{r}')$ ) with the system impulse response  $h$ . The image formation algorithm is then fundamentally an inverse convolution process which can be implemented as a correlation,

$$\zeta(\vec{r}) = \int_{\text{time footprint in data}} h^{-1}(\vec{r}_{sc}(t, i) - \vec{r}) V_{bb}(\vec{r}_{sc}(t, i)) dt di \quad (29)$$

where  $h^{-1}$  is the inverse Green's function which is given by the matched filter for the impulse response  $h$ . The matched filter in this case is the complex conjugate of the impulse response,

$$h^{-1}(\vec{r}_{sc}(t, i) - \vec{r}) = h^*(\vec{r}_{sc}(t, i) - \vec{r}) \quad (30)$$

where  $h^*$  denotes the complex conjugate of  $h$ . The time footprint in the data is the range gate time for  $t$ , and the synthetic aperture time for  $i$ . The normalized radar

cross-section is estimated from the complex reflectivities by squaring the magnitude,

$$\sigma_0(\vec{r}) = \langle |\zeta(\vec{r})|^2 \rangle, \quad (31)$$

where  $\sigma_0(\vec{r})$  is the normalized radar cross-section at position  $\vec{r}$  on the surface. The dimensionless normalized radar cross-section is related to the single scatterer radar cross-section ( $\sigma$ ) with units of area that appears in (24) by taking the average of  $\sigma$  over many scatterers and dividing by the surface area occupied by these scatterers.  $\sigma_0$  is the fundamental measured quantity needed by the soil moisture retrieval algorithms.

## 7.2 High Level Algorithm Organization and the Direct Correlation Algorithm

The L1C process begins with the formation of the output grid tailored for the current data granule. All the peg points are determined along with the coordinates of the 1 km output cells. In addition to the output grid at 1 km spacing, a full resolution grid with 200 m spacing is also set up. The full resolution grid will accumulate single look resolution cells from each conical scan of data. The sizes of these grids in memory are determined by the forward and backward swath row time ranges discussed earlier. The grids will likely be held as circular buffers with new rows added in the direction of motion as needed, and completed rows written out to file and removed from memory when no longer needed. The basic loop of the processor will be over full resolution grid rows as shown in fig. 8. For each output row, the time extent of telemetry data that can contribute to it will be determined and loaded from the input L1A file. Again, circular buffers will likely be used to hold the time domain telemetry data which will cover the forward and backward swath row times. Once loaded, the raw BFPQ radar samples will be decoded into floating point complex (I,Q) samples. After BFPQ decoding, the radar data are noise subtracted using the current noise power model derived from the noise channel data, and gain corrected for short term gain variations using the gain correction model derived from loop back measurements. Following this the baseline RFI detection/correction algorithm is applied. Then the radar samples are correlated in range and azimuth to produce spatially ordered results with single look resolutions of 236 m by 400-1200 m. Several algorithm choices are available for this step. The most basic is a direct correlation which will be implemented as a reference to test the accuracy of faster operational algorithms. The direct correlation algorithm simply constructs the point target response using (23) for a point located at the center of each grid square over the range gate and synthetic aperture times and correlates this with the corresponding data recorded in the receive windows as specified by (29). The data are discretely sampled in  $t$  by the 1.25 MHz sample rate, and  $i$  is naturally

discrete with PRI spacing, so the integration in (29) is implemented as two nested summations,

$$\zeta(\vec{r}) = \sum_i \sum_k h^*(R(k * \tau_s + i * \tau_{pri}))D(t, i), \quad (32)$$

where  $\tau_s = 1/f_{ctu}$  is the sample period of the high-res data,  $R(k\tau_s + i\tau_{pri})$  is the range from the spacecraft at the sample time  $k\tau_s$  within pulse  $i$ , and  $D(t, i)$  is the data sample at that same sample time and pulse. The correlation picks out the energy in the data that has the same range and Doppler variation as the desired point target. The summation range of  $i$  is the synthetic aperture time for the target at position  $\vec{r}$ . The synthetic aperture time will nominally contain all the pulses that illuminate the target point within some specified level (eg., -3 dB of the peak) of the antenna main lobe. This time interval may be varied around the conical scan to optimize ambiguity performance. The summation range of  $k$  is the range gate time for the target at  $\vec{r}$  during pulse  $i$ . In principle, the summation range of  $k$  could be a function of  $i$ , but for SMAP, the synthetic aperture time is fairly short so a single range may suffice for  $k$ . After evaluating the summations for all of the desired grid cells, we use (31) to convert the result to  $\sigma_0$  for the resolution cell centered on the grid cell center point. The resolution cell is approximately a parallelogram on the surface that covers the range and Doppler spread of the impulse response. To ensure that all energy is captured, this process is performed on the full resolution grid (200 m spacing). Although the direct correlation algorithm is relatively simple to implement and makes no simplifying assumptions, it is not very efficient because the correlation has to be performed over all 120 receive windows within the synthetic aperture time for every grid square in the full resolution grid. An operational algorithm will likely need to be much faster. Two choices for an operational algorithm are being evaluated. The rectangular algorithm assumes that the range and azimuth correlations can be decomposed into two 1-D matched filters applied in succession. Due to the short synthetic aperture time (38 ms), range cell migration is expected to be small and probably negligible, so this algorithm may work well enough. Range cell migration may become noticeable for the inner portion of the swath where the range rate along the look direction is highest. If needed, an interpolation correction for range cell migration can be included before the final azimuth matched filter. The SPECAN algorithm (see Ch. 10 in [12] and Ch. 9 in [15]) is an alternative which simplifies the azimuth processing step down to a frequency filter.

While the direct correlation algorithm produces results directly in the output swath grid, the rectangular and SPECAN algorithms will produce results evenly spaced in range and Doppler. These algorithms will then require an additional step to reproject or interpolate their output onto the swath grid. In the following subsections, the rectangular or SPECAN algorithms are assumed. Once range-Doppler pixels are obtained, the image data are multi-looked and located on the Earth's sur-

face. Radiometric calibration is applied using a combination of geometry data and measured system parameters. Long term gain corrections are applied to the image data using a model built up from reference target data. The low resolution processing flow does not include range or azimuth compression, but does include the geolocation and radiometric calibration steps.

### 7.3 BFPQ Decoding

The first step inside the main loop shown in Fig. 8 is BFPQ decoding. The raw samples produced by the onboard digital filtering and quadrature demodulation are 16 bits with an effective sample rate of 1.25 MHz. These are reduced by a block adaptive floating point quantizer (BFPQ) algorithm [9] to 4 bit samples with 5 bit exponents generated for each block of 32 samples in a receive window. Depending on PRI, the number of these 32-sample blocks varies from 9 to 14. These parameters are selected to reduce data volume while still meeting the overall error budget. The LIC processor will decode the BFPQ samples on the fly as data are processed. The algorithm is designed to have unity gain and should not introduce any bias for normal data with gaussian error statistics. RFI contamination can change this and will require a bias correction described later.

### 7.4 Geometry Processing and Interpolation

SAR processing needs certain key geometric information to form the matched filters and to calibrate the output image pixels. Some geometry processing can be pre-computed by the LIC processor with results stored either in memory or in an intermediate file. The key values will be the range and Doppler and their time derivatives at the center of each output grid cell on the current SCH reference sphere. The range  $R$  to a given position  $\vec{r}$  on the surface is given by (26), and the Doppler shift of a target at  $\vec{r}$  is

$$f_{Dc} = \left(\frac{-2}{\lambda R}\right)(\vec{v}_{sc} \cdot (\vec{r}_{sc} - \vec{r})) \quad (33)$$

Earth fixed coordinates are used to automatically account for the effects of Earth rotation. For calibration, the attitude transformation matrix from Earth fixed coordinates to beam pattern coordinates which rotate with the antenna will be needed to determine the antenna gain correction. These values computed at some coarse spacing by the LIC processor will then be interpolated to the individual pulse and sample times needed for range and azimuth compression.

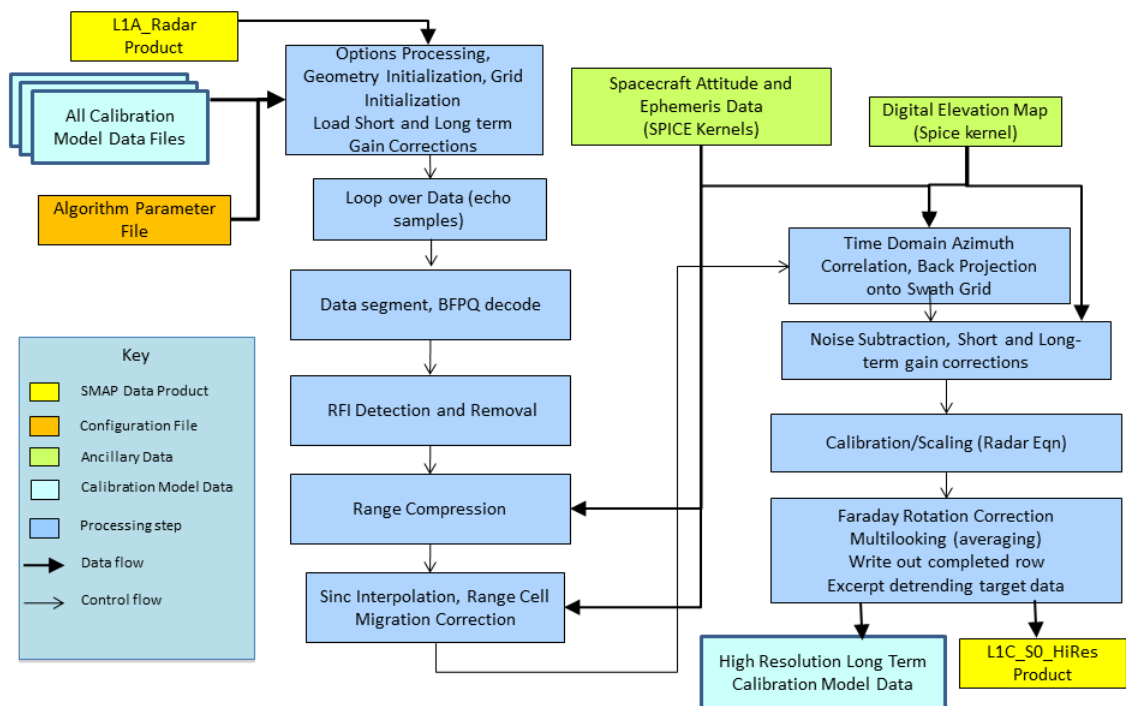


Figure 8: L1C Processing flow diagram. This diagram shows the rectangular algorithm. Processing loops over the input range lines (pulse echoes) Range compression is performed first, and then the contribution to the time domain azimuth correlation is back projected onto the swath grid. The processor keeps data in memory covering the current position of the conical scan. Output arrays are held in memory and written out at the end of processing.

## 7.5 Range Compression

Range compression consists of the convolution of each range line with the complex conjugate of the pulse form (in the frequency-domain). The range reference function is calculated in the time-domain using the pulse form characteristics (pulse bandwidth, pulse duration, sampling frequency) given by the radar instrument team, and is transformed to the frequency domain using a FFT. A user-defined window can also be applied to reduce the sidelobes of the impulse response in range. For each range sample, timing is transformed into slant range, taking into account a possible sample timing offset. Slant range values stay the same as long as the PRF and reception window timing remain constant, which is assumed to be the case for a full antenna scan. Loopback trap data provide a periodic sampling of the actual transmit pulse waveform, and it may prove advantageous to use this measurement as the reference function. The LIC processor will be built with both options selectable using a processing configuration parameter.

With the time-bandwidth product now reduced to 15, it may be more efficient to implement range compression with a direct time-domain correlation rather than the FFT based convolution algorithm described above. These choices need to be evaluated with simulated data to see which provides the best trade-off between accuracy and execution speed.

### 7.5.1 RFI

Detection and removal of interferences within the SAR images will be necessary for SMAP since the L-band frequency is widely used by ground radars. The baseline algorithm will involve applying a threshold to the data either just before or just after range compression and then replacing contaminated data with a replica from an adjacent pulse echo. Additional details are described in the RFI section of this document.

## 7.6 Azimuth Phase Correction

The SMAP radar is designed to hop its transmit frequency by 1.25 MHz steps within an allowed 80 MHz wide spectrum at L-band. This is done to help avoid RFI contamination by hopping to relatively clear bands depending on orbit location and scan direction, and also to prevent potential interference by the SMAP radar to FAA operated radars on the ground. The frequency hopping is implemented by stepping the frequency of the digital chirp generator, and the frequency of the mixdown RF to IF stage. The baseline design will step the PRI by  $0.8 \mu\text{s}$  which is the reciprocal of the frequency step size, thus ensuring a completely phase coherent system. However, the system will have the capability to step the PRI by  $0.1 \mu\text{s}$  in case the extra

precision is needed to keep the echo windows centered against range variation due to attitude errors along with the expected range variation due to the non-spherical shape of the Earth, the eccentricity of the orbit, and topography. If this option is used, then a deterministic phase progression will occur from pulse to pulse which will need to be corrected by ground processing before azimuth compression can be performed. The phase offset will have the form

$$\text{phase progression remainder} = \text{mod}\left(\frac{-in_1m_d}{8}, 1\right) \quad (34)$$

where  $i$  is an integer pulse index, and  $n_1$  and  $m_d$  determine the PRI and the mix-down frequency as described earlier. This correction will be applied by multiplying a complex exponential to each range line with the appropriate phase progression remainder before performing azimuth compression.

## 7.7 Azimuth Compression

The conical scan used by SMAP produces a very high Doppler rate during the synthetic aperture times. This means that the operational azimuth compression will likely be performed in the time-domain. Studies conducted for Hydros indicated that frequency-domain matched filtering cannot be considered in the SMAP case since the Doppler center frequency changes constantly in slow time due to the rotation of the antenna. This will be verified and may preclude the use of SPECAN and other more sophisticated frequency domain algorithms. A time-domain procedure can be considered in this case because the time in view of each target is short (about 37 ms) and so are the length of the convolutions (about 100 samples), making the computation load viable. A time-domain algorithm is a direct implementation of the focusing procedure. Each azimuth compressed pixel is obtained by combining samples at the same slant range in a group of consecutive pulse-compressed range lines. This combination is a weighted sum of the samples multiplied by the compression coefficients given by the azimuth reference function  $h_{az}^{-1}$ ,

$$h_{az}^{-1} = \exp(-j2\pi(f_{Dc}s + f_R \frac{s^2}{2})) \quad (35)$$

with  $s$  being the pulse time (slow time) given by,

$$s = (i - i_0)\tau_{pri} \quad (36)$$

where  $i_0$  is the pulse index at the center of the synthetic aperture time being processed. The weighting comes from the antenna pattern variation in the azimuth direction, and the number of pulses in the weighted sum is determined by the azimuth processing bandwidth which may be varied with scan position. The effect

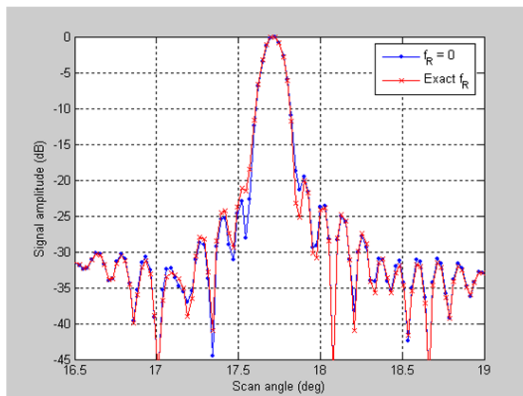


Figure 9: Azimuth cut of the processed image of a point target ( $\approx 18^\circ$ ) with and without  $f_R$  in the focusing

of the Doppler rate  $f_R$  in Equation 35 is expected to be negligible in the focusing procedure because of the short time in view (Fig. 9 and Fig. 10). Neglecting the Doppler rate allows a pre-computation of the compression coefficients for Doppler centroid  $f_{Dc}$  values between 0 and PRF. The compression coefficients can then be extracted from a lookup table, improving the throughput.

A high precision is needed for the Doppler centroid calculation for a rotating SAR because an error on  $f_{Dc}$  causes an error on scanning angle and then a displacement of the target location on the ground. Since topographic variation from the reference sphere affects the Doppler centroid calculation, a digital elevation model (DEM) will be included in geometric calculations. The effect is more important at scan angles of  $18^\circ$  (inner edges of the nominal swath), where an error on  $f_{Dc}$  of only 2.5 Hz corresponds to a geolocation error of 100 m. At  $90^\circ$ , a Doppler frequency error of about 8 Hz corresponds to a geolocation error of 100 m. Since the synthetic aperture time is very short, the range cell migration effect is expected to be negligible. There is only a small impact (about 5% broadening) for very low scan angle (near  $18^\circ$ ) as seen on Figure 11 and Figure 12. The samples used for azimuth compression could then be extracted column-wise in the complex matrix containing the range-compressed signal.

## 7.8 Terrain-Corrected Geolocation

The direct correlation approach will automatically geolocate the output image pixels because the reference functions are formed for a specific output grid cell. The Rectangular and SPECAN algorithms form the image in the range Doppler domain which then needs to be transformed to image coordinates. As mentioned in the

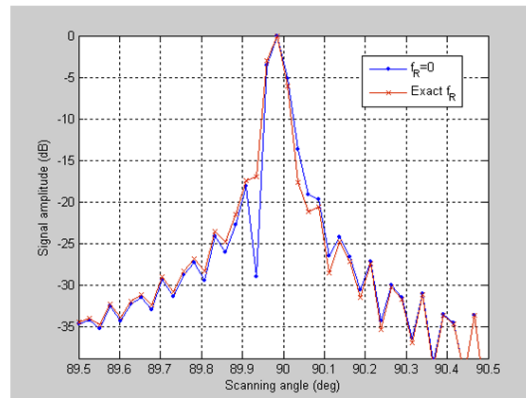


Figure 10: Azimuth cut of the processed image of a point target ( $\approx 18^\circ$ ) with and without  $f_R$  in the focusing

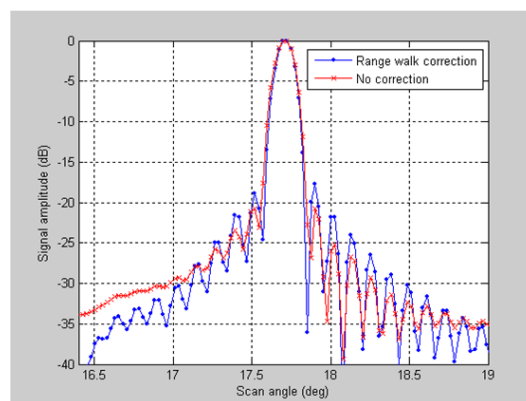


Figure 11: Processed image (azimuth) of a point target near ( $18^\circ$ ) with and without range walk correction.

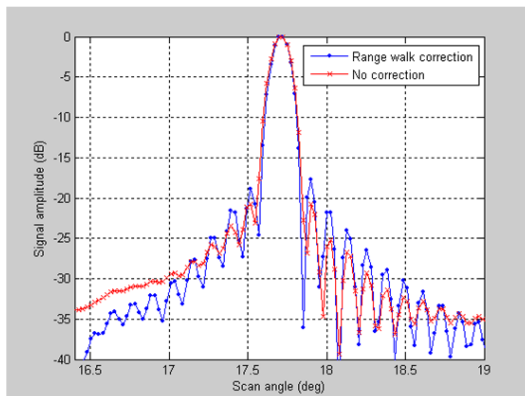


Figure 12: Processed image (azimuth) of a point target near broadside with and without range walk correction.

prior section, this step could be done during azimuth compression to improve the precision on the Doppler centroid. Geolocation consists of finding the location on Earth of a pixel specified by a particular slant range and Doppler shift. This is done separately for each range line by using orbit data and topography data. The procedure consists of finding the simultaneous solution for the 3 cartesian coordinates ( $x,y,z$ ) of three equations: slant range equation, Doppler equation, and Earth model equation (including height  $h$  above the reference spheroid). Solving this nonlinear system (with some iteration needed for topographic corrections) for every output pixel may be prohibitively time consuming, so it may be necessary for the LIC processor to precompute and tabulate values for interpolation. More study is needed here to see what the tradeoffs between speed and location accuracy will require while still meeting the basic location accuracy of 1 km.

## 7.9 Image Calibration using Radar Equation

In this processing stage, the output of the correlation processing is scaled to  $\sigma_0$  values using the X-factor (radar equation) calculation described in the next section, along with any processing gain factors and multiplicative noise corrections needed. The scaling factors will vary significantly around the scan. Results in the nadir gap will likely require special handling.

## 7.10 Regridding and Multi-Looking

As single look resolution cells are geolocated, they can be accumulated directly to the output swath grid using the SCH coordinate system to define the map pro-

jection. This approach is similar to the multi-looking approach used by Cassini RADAR processing and Magellan processing, but different from other SAR processors like SRTM that form a multi-looked image in the range-Doppler domain and then transform to the output image domain. For SMAP, there is no reason to keep data in the range-Doppler domain, and this direct conversion approach should be most efficient. A given set of geographic coordinates in the SCH frame is converted to along track and cross track distance using the radius from the most recent peg point. A zero point for the along track coordinate will need to be established, probably at the start of the data take. Single look resolution cells whose centers fall in the same output swath grid square are averaged together. An area weighted average will be used so that resolution cells that only fall partially in the output swath grid square will be weighted less than fully contained cells.

## 8 L1B Processing Algorithms

Low resolution data are derived from the same high resolution samples used by the SAR processing. To save downlink data volume, the initial processing steps are performed by the radar instrument itself, with summary results placed in the Low-res packets for downlink. The radar divides each receive window into 32 sample blocks (the same blocks used for BFPQ encoding) and sums the powers ( $I^2 + Q^2$ ) in each block. Depending on the PRI value in use, the receive window will be binned into 9-13 range bins. The last block can have less than 32 samples. Each range bin contains echo power from a rectangular slice area on the surface with projected range resolution of about 5 km. These range slices are downlinked in the low-res packets for both co-pol and both cross-pol channels along with averaged noise channel data for each PRI. The core algorithms of the L1B processor locate each range slice on the Earth's surface and scale the echo power by the antenna gain variation experienced by each slice. The L1C processor will also sum the slice measurements to obtain a total footprint measurement. The total footprint measurement is located by the boresight intercept position on the Earth's topographic surface. For the slice measurements, the geolocation algorithm will perform an iterated search along each beam azimuth edge for the start and end of each range bin taking into account the topographic surface supplied by the DEM. These four points then define a rectangular region or slice which reflects back most of the echo energy contributing to a range bin measurement.

After geolocating the measurements, the L1B processor will subtract an estimate of the noise power, and then apply scaling to convert the measurement from a power estimate to a normalized backscattering cross-section ( $\sigma_0$ ). Finally, antenna cross-talk and Faraday rotation corrections are applied using the 4 available polarimetric measurements.

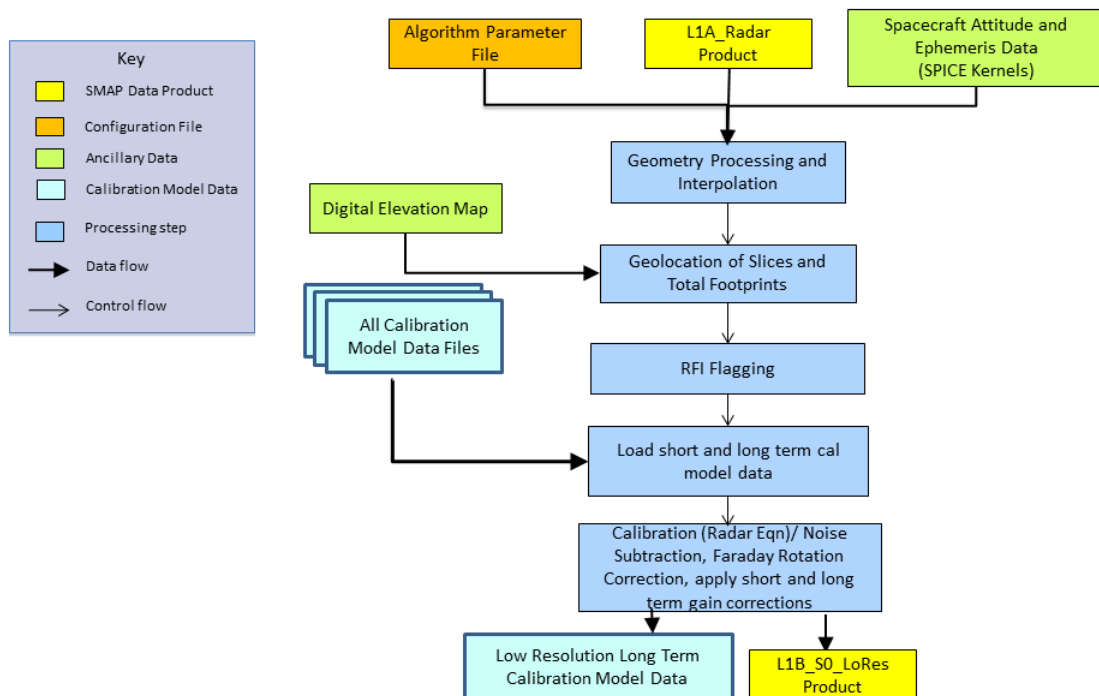


Figure 13: L1B Processing flow diagram. L1B processing starts with low-res data from the radar which have already been averaged over range bins corresponding to the BFPQ blocks used by the high-res data. The L1B processing flow proceeds in time order, applying calibration, geolocation processing, and noise subtraction. RFI is flagged, but not corrected. The main differences from L1C processing are the absence of SAR correlation processing, and the need to integrate the beam pattern over each range slice footprint when applying the radar equation.

## 8.1 Noise Subtraction

The radar instrument reports sums of  $I^2 + Q^2$  over low-res intervals which contain 48 PRI's. These sums contain both signal power from reflected echoes, and noise power from the instrument electronics and from surface emission. Noise channel measurements are provided along with the range bin measurements to estimate the noise power level separate from the signal power. The noise channel measurements are provided for each of the 48 PRI's separately to allow for RFI detection with greater resolution than a low-res sum would provide. The L1A SPS converts the raw low-res measurements to power measurements in units of dBm. For noise subtraction, the noise measurements are converted from dBm to Watts and averaged over the 48 PRI in a LRI. The signal+noise measurements have already been averaged by the L1A SPS, so they are simply converted to Watts before subtracting the noise.

## 8.2 Radar Equation Scaling

The normalized backscattering cross-section  $\sigma_0$  is related to the received power by the radar equation (Sec. 7.16, [8]),

$$P_s(t) = \frac{\lambda^2}{(4\pi)^3} \int_A \frac{P_t(t - \frac{2R}{c}) G_{at}(t - \frac{2R}{c}) G_{ar}(t) \sigma_0}{R^4} dA, \quad (37)$$

where  $P_s(t)$  is the instantaneous received signal power referenced at the antenna port at time  $t$ ,  $\lambda$  is the transmitted wavelength,  $A$  is the illuminated area on the surface,  $P_t(t)$  is the radiated transmit power pulse train,  $G_{at}$  and  $G_{ar}$  are the antenna transmit and receive gains at the corresponding transmit and receive times respectively,  $\sigma_0$  is the normalized backscattering cross-section, and  $R$  is the range to the surface. To derive the proper radar scaling equation for real aperture results, we need to average the received signal power over range bins and pulses in the same way that the echo buffer data are summed by the instrument and noise subtraction processing when forming  $\langle D_s \rangle$ . The average received signal power for range bin  $k$  is given by,

$$\langle P_{sk} \rangle = \frac{1}{N_p n_k \tau_s} \int_0^{\tau_k} \sum_{i_s=0}^{N_p-1} P_s(t - i_s \tau_{pri} - k \tau_k) dt \quad (38)$$

where  $\tau_k = n_k \tau_s$  is the time width of range bin  $k$ , and  $\tau_s = 1/f_s$  is the sample period.

The transmitted pulse train for a low-res measurement is given by,

$$P_t(t) = P_{t0} \sum_{i_s=0}^{N_p-1} u_p(t - i_s \tau_{pri}), \quad (39)$$

where  $P_{t0}$  is the transmit power level during a pulse transmission,  $N_p$  is the number of pulses summed by the instrument in a low-res interval (48), and  $\tau_{pri}$  is the pulse repetition interval.

Substituting (37) and (39) into (38) and reversing the order of integration gives,

$$\langle P_s \rangle = \frac{\lambda^2}{(4\pi)^3} \frac{P_{t0}\sigma_0(\theta_i)}{R_0^4} \frac{1}{\tau_{rb}} \int_A \int_0^{\tau_{rb}} \sum_{i=0}^{N_p-1} u_p(t - i\tau_{pri} - \frac{2R}{c}) u_{rw}(t) G_{ar} G_{at} dt dA. \quad (40)$$

Here we have assumed that variation of range within the integral is insignificant and variation of backscatter over the range of incidence angles within the integral is unmodelled. The general values are pulled out of the integral and replaced by the range to the center point  $R_0$ , and the normalized backscatter at the center incidence angle  $\sigma_0(\theta_{i0})$ . If the receive window covers all of the echo power including range spread, then the time integral over the pulse train summation can be simplified to the number of pulses  $N_p$  multiplied by the integral over one pulse. The time integral over one pulse then evaluates to just  $\tau_p$  and we have,

$$\langle P_s \rangle = \frac{\lambda^2}{(4\pi)^3} \frac{P_{t0}\sigma_0(\theta_i)}{R_0^4} \frac{N_p\tau_p}{\tau_{rb}} \int_A G_{ar} G_{at} dA \quad (41)$$

### 8.2.1 Scan Loss

The illuminated area integral needs to account for motion of the antenna beam as indicated by the time arguments to the transmit and receive gain factors. We define a scan loss factor to account for the motion of the antenna beam as follows,

$$G_{at}(t - \frac{2R}{c}) G_{ar}(t) = G_{at}(t) G_{ar}(t) G_{sl}(\frac{2R}{c}). \quad (42)$$

Here we assume that the scan loss factor  $G_{sl}$  is only a function of the round trip time which is held constant because the instrument maintains a constant look and incidence angle. Small variations due to topography and the ellipsoidal shape of the Earth are neglected so that the scan loss factor can be computed once at the start of processing.

## 9 Calibration

Radiometric calibration of the SMAP radar means measuring, characterizing, and where necessary correcting the gain and noise contributions from every part of the system from the antenna radiation pattern all the way to the ground processing algorithms. The important elements are shown in Fig. 14

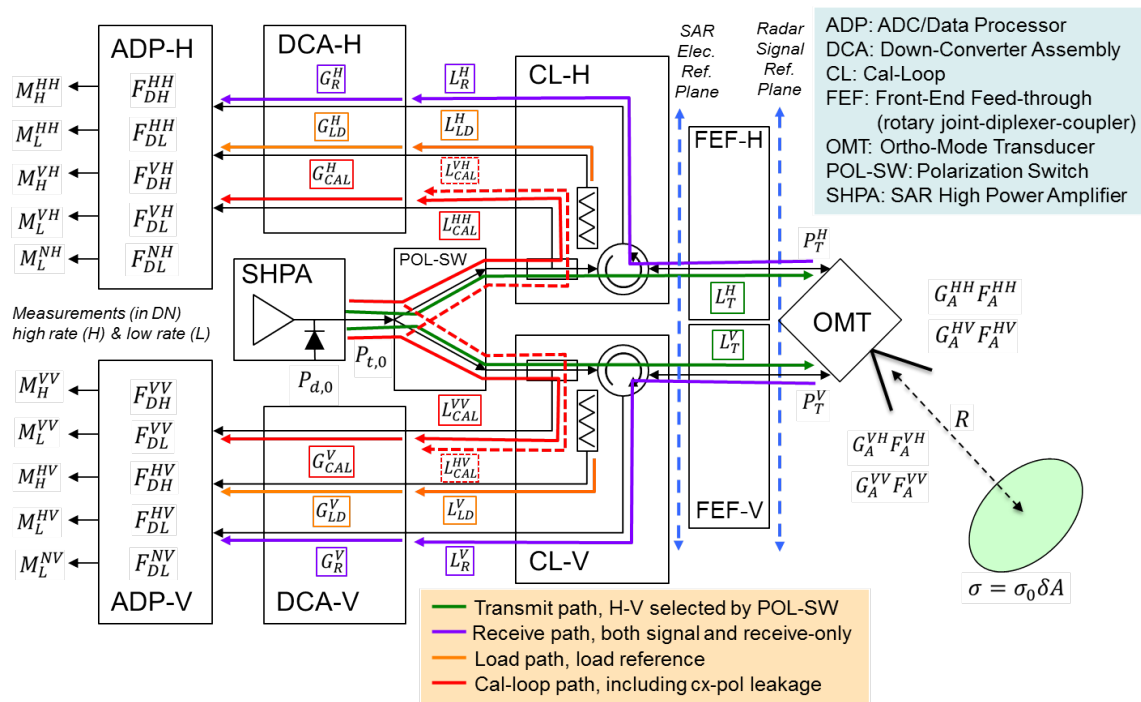


Figure 14: Simplified system diagram showing the loop-back path and the main elements that affect calibration. Passive components with loss are denoted with L, active components with possible gain are denoted with G, and digital processing path gains are denoted as a function F. Different paths are color coded according to the legend.

## 9.1 Antenna Gain Pattern

Knowledge of the antenna gain pattern will be important to both active and passive calibration. The SMAP antenna pattern will be computed using an accurate antenna model. During early development of ground software, a  $\text{sinc}^2$  pattern characteristic of a uniformly illuminated aperture will be used for simulation and testing. The beamwidth will be set to the nominal half-power beamwidth of 1.9 (TBC) degrees.

## 9.2 Receiver Gain and Noise Temperature

The radar receiver will produce its own internal noise which arises from thermal fluctuations in the RF components. Most of the noise is produced in the front-end where signals receive the highest amplification. The noise counts ( $V_n$ ) can be described in terms of an effective receiver noise temperature ( $T_r$ ) and an overall receiver gain ( $G$ )

$$V_n = G(T_r + T_a), \quad (43)$$

where  $T_a$  is normally the antenna temperature due to thermal emission from the observed scene. Variations of  $G$  will occur as the physical temperature of various system components vary. Matched load measurements are collected by SMAP once per antenna revolution. Cold space measurements will be taken monthly for radiometer calibration. Radar processing can take advantage of these measurements to determine the receiver gain  $G$  when both matched load and cold space measurements are taken together. The matched load measurement by itself can be monitored to give some indication of gain and/or noise temperature drift.

The product of transmit power  $P_t$  and receiver gain  $G$  are measured every PRI by a loopback measurement which is reported with the low-resolution data in the telemetry stream. These data will be averaged over a time span specified by a processing configuration parameter. The averaging time will be selected to minimize the statistical variance of the loopback measurement while still tracking variations of transmit power and receiver gain. These variations are expected due to component temperature variations that will occur as the spacecraft orbits the Earth. The loopback measurement is then used to divide out the short term gain variability in the affected data.

## 9.3 Statistical Measurement Uncertainty and Noise Subtraction

The radar equation relates the received signal power  $P_s$  to the radar backscattering cross-section ( $\sigma_0$ ). The radar instrument, however, measures a combination of the received signal power and internal noise power

$$P_{sn} = P_s + P_n \quad (44)$$

where  $P_n$  is the internal thermal noise power. Ground processing will estimate the internal noise power using noise only measurements and subtract this from the raw signal+noise measurements. The resulting estimate of  $P_s$  is subject to statistical error from both  $P_{sn}$  and  $P_n$  which is given by [10]

$$K_{pc}^2 = \frac{1}{N\tau_p B} \left(1 + \frac{2}{\text{SNR}} + \frac{1}{\text{SNR}^2}\right) \quad (45)$$

where  $N$  is the number of pulses averaged together,  $\tau_p$  is the pulse width, and  $B$  is the measurement bandwidth.

Both  $K_{pc}$  and  $N$  vary as a function of scan position or cross-track position.  $K_{pc}$  also varies as a function of SNR which depends on the scene being observed. The requirements are generally applied for the worst case position which is the inner edge of the usable swath for  $K_{pc}$ , and assuming the average scene backscatter level matches the designated minimum  $\sigma_0$  level of -25 dB. Figures 15 and 16 show the variation of looks ( $N$ ) and  $K_{pc}$  as functions of cross track distance. The inner edge of the usable swath occurs at 150 km cross track distance, while the outer edge lies at 500 km cross track distance. Additional details on these performance parameters and how they relate to requirements are available in a preliminary calibration report [7].

## 9.4 Radar Equation and Error Budget

The normalized backscattering cross-section  $\sigma_0$  is related to the received power by the radar equation (Sec. 7.16, [8]),

$$P_s(t) = \frac{\lambda^2}{(4\pi)^3} \int_A \frac{P_t(t - \frac{2R}{c})u_{rw}(t)G^2\sigma_0}{R^4} dA \quad (46)$$

where  $P_s(t)$  is the received signal power referenced at the antenna port at time  $t$ ,  $\lambda$  is the transmitted wavelength,  $A$  is the area on the surface illuminated by the antenna main lobe,  $P_t(t)$  is the radiated transmit power pulse train,  $u_{rw}(t)$  is the receive window filter,  $G$  is the antenna gain (neglecting transmit receive differences due to spacecraft motion during the round trip time),  $\sigma_0$  is the normalized backscattering cross-section, and  $R$  is the range to the surface. The receive window filter is defined by

$$u_{rw}(t) = \begin{cases} 1 & \text{for } \tau_{rwd} < t < \tau_{rwd} + \tau_{rw} \\ 0 & \text{otherwise} \end{cases} \quad (47)$$

where  $\tau_{rwd}$  is the delay from the start of a transmitted pulse train to the time the receive window is opened and the receiver begins digitizing echo power, and  $\tau_{rw}$  is the duration of the echo buffer.

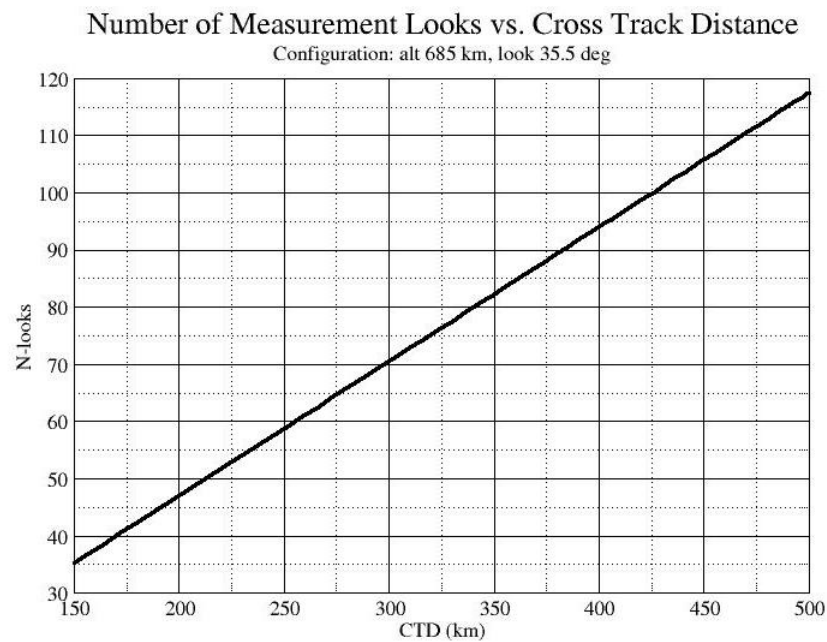


Figure 15: Plot of the total number of measurement looks in a 3 km by 3 km measurement cell vs cross track distance (CTD). The inner edge of the usable swath occurs at 150 km CTD, and the outer edge at 500 km CTD. This plot shows all looks from a single scan, including forward and backward looks, but not including multiple scans which will add some looks for the outer edge area.

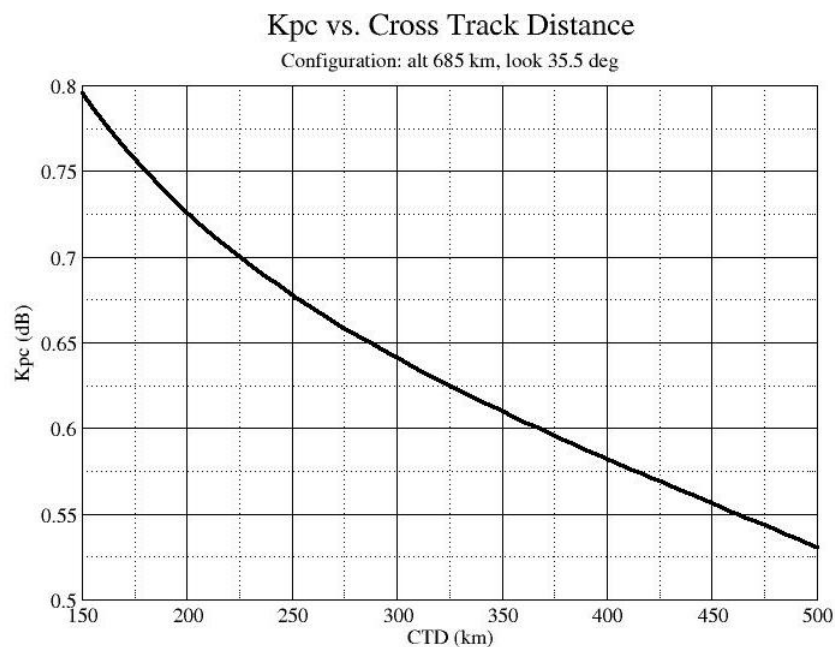


Figure 16: Plot of the normalized measurement standard deviation ( $K_{pc}$ ) for a 3 km by 3 km measurement cell vs cross track distance (CTD). The inner edge of the usable swath occurs at 150 km CTD, and the outer edge at 500 km CTD. This plot shows results for a minimum  $\sigma_0$  value of -25 dB, and assumes only looks from one half of the scan are used. The quantity plotted is actually  $10 \log_{10}(1 + K_{pc})$  following the common practise for scatterometer measurements.

For SAR processing, the real aperture integral can be simplified neglecting parameter variation over the small size of a single resolution cell.

$$P_s = X\sigma_0 \quad (48)$$

$$X = \frac{\lambda^2}{(4\pi)^3} \frac{P_t G_a^2 G_c G_r C_{adc} A_{res}}{R^4} \quad (49)$$

where  $P_t$  is the average transmit power during the pulse,  $G_a$  is the effective one-way antenna gain at the range of the resolution cell,  $G_c$  is the compression gain from range and azimuth compression processing,  $G_r$  is the receiver gain,  $C_{adc}$  is the translation factor of ADC sample counts per Watt,  $A_{res}$  is the surface area of the resolution cell, and  $R$  is the range to the resolution cell. The effective antenna gain  $G_a$  is obtained by integrating the antenna pattern as occurs in azimuth compression processing.

Equation 48 shows that  $\sigma_0$  depends on  $P_s$  and  $X$ , so the error of  $\sigma_0$  will be the sum of the statistical measurement error in  $P_s$  termed  $K_{pc}$  (see Equation 45), and the uncertainty of  $X$  termed  $K_{pr}$ , or the calibration error. The calibration error is the sum of the uncertainties in each of the factors in Equation 49 plus some long term detrending uncertainty described in the next section. Table 12 summarizes the key contributors and allocations to the  $\sigma_0$  error budget and table 13 further breaks down the radiometric calibration error. The  $K_{pc}$  allocation applies at the inner edge of the usable swath. Additional detailed information on the overall error budget is available in the preliminary calibration report [7].

Table 12: High Level Summary Error Budget

Parameter	Error Allocation
$K_{pc}$ , Statistical measurement error	0.72 dB
$K_{pr}$ , Radiometric calibration error	0.40 dB
$K_{prfi}$ , RFI contamination error	0.40 dB
Total (RSS)	0.92 dB
Requirement	1.0 dB
Margin (linear)	0.08 dB
Margin (RSS)	0.40 dB

## 9.5 Long Term Detrending

Short term variations in various gain and loss factors that affect  $\sigma_0$  calibration are expected to be correctable within the limits specified by the error tables in the previous section. These corrections will use built-in calibration measurements, such

Table 13: Calibration Error Table

Parameter	Error Allocation	Calibration Method
$\lambda^2$	< 0.01 dB	Design, Could verify with clock drift measurement
$R^4$	< 0.01 dB	Nav/Ephemeris determination
$G_a$ - pointing errors	0.22 dB	Pre-launch measurement, pointing stability reqmt
$G_a$ - feed, antenna stability	0.07 dB	Pre-launch measurement, antenna stability reqmt, post launch antenna model fitting
$P_t G_r$	0.1 dB	Internal loopback measurements
$L$ - outside of loopback	0.1 dB	Pre-launch temperature models, post-launch correction
$L$ - shared components (rotary joint, feeds)	0.1 dB	Pre-launch temperature models, post-launch correction
$P_s$ - noise subtraction	0.1 dB	Design, noise only data
$P_s$ - ambiguity/PSF contamination	0.1 dB	Design, noise only data
$P_s$ - Faraday rotation	0.1 dB	Use radiometer derived correction
$A_{res}$	0.1	Processing algorithm
RSS of above terms	0.35	Applies on short (1 month) time scale
$X$ - long term variability	0.2	Use reference target (Amazon) to track
RSS of above two terms	0.4	Total $K_{pr}$

as the loop back measurement performed every PRI, and pre-launch temperature dependence models along with temperature measurement telemetry to remove gain and loss variations. Due to limited testing time and resources, it is not possible to guarantee that these models and corrections will work within requirements over the lifetime of the mission. It is expected that seasonal and longer term temperature variations, and component aging and degradation, will introduce long-term trends and biases into the  $\sigma_0$  results. To reduce these effects below their error allocation, data will be collected over known stable target areas and then used to correct for long-term variability. The baseline reference target is part of the Amazon rain forest which has been used successfully by several past missions at both L-band and Ku-band. Figure 17 shows an L-band image of the Amazon area along with a target area analyzed during the JERS-1 mission. Table 14 summarizes published results [11] on the stability of the H-pol L-band radar backscatter in the target area. These data were taken over a 6-year time period and show stability to within 0.2 dB if the dry and wet seasons are separated.

Season	Mean $\sigma_0$ (dB)	SD	Mean $\gamma_0$ dB	SD
All	-6.92	0.23	-5.83	0.23
Dry	-7.08	0.18	-5.99	0.18
Wet	-6.81	0.20	-5.72	0.20

Table 14: Summary of L-band SAR normalized radar cross sections. Here,  $\gamma_0 = \sigma_0 / \cos \theta$  with  $\theta$  being the measurement incidence angle[11].

Although these data only apply to copolarized H-pol  $\sigma_0$ , VV data are expected to show similar or better stability. This expectation is based on the observation that the primary cause of the L-band variability is flooding and according to scattering theory, H-pol data should be the most sensitive to scattering off of surface water. Cross-pol data are also expected to show better stability, although at a lower backscatter level which is harder to measure. PALSAR polarimetric data will be collected and analyzed to further verify expectations of the stability of the Amazon backscatter levels.

Alternate reference targets include the oceans (with a suitable wind correction model) and the large terrestrial ice sheets in Greenland and Antarctica. These targets could also potentially be used for long term detrending.

## 9.6 Absolute Calibration

The calibration procedures discussed so far address the issue of relative calibration or stability of the measurements. Even after all of the short and long term variations

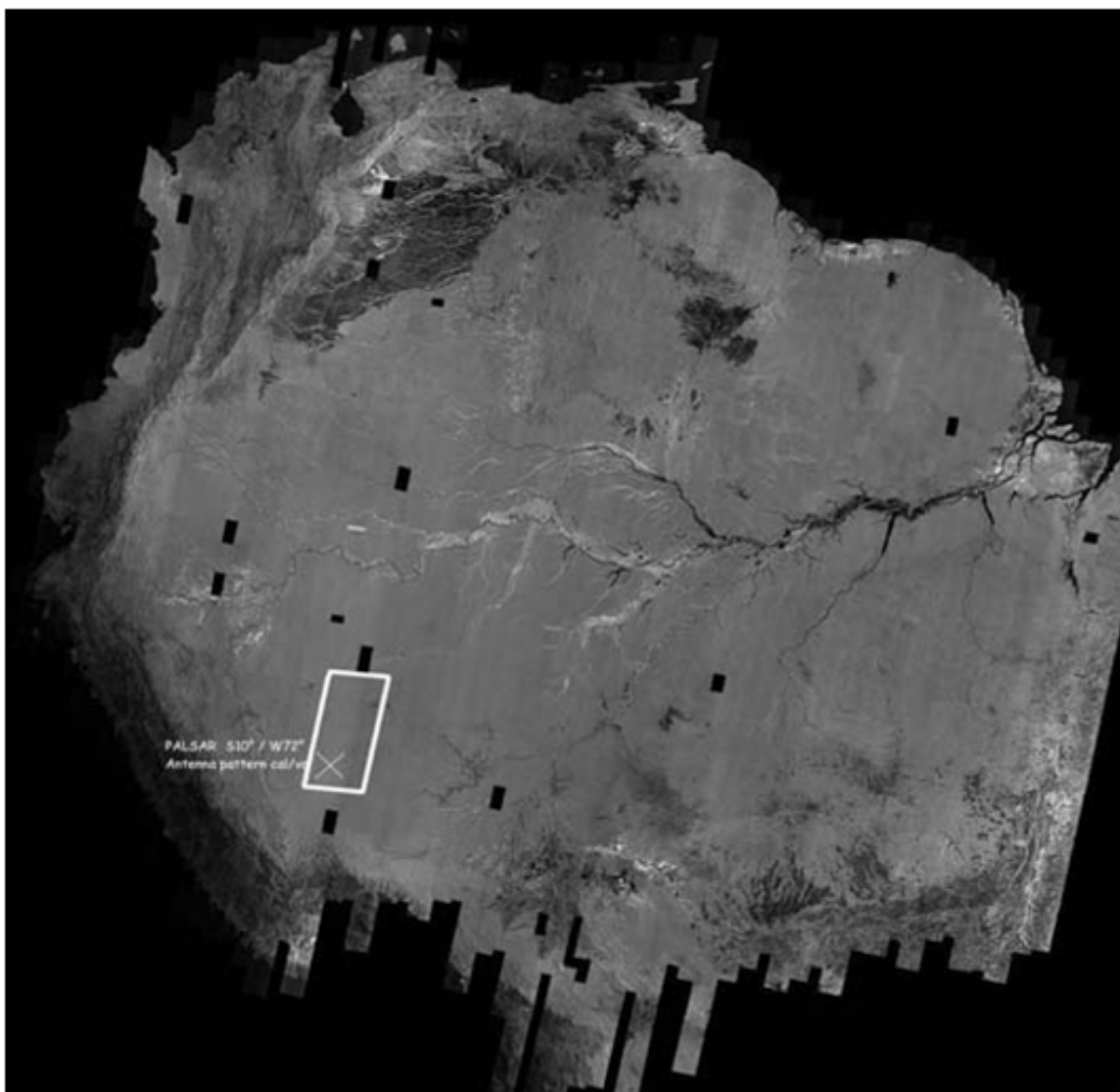


Figure 17: JERS-1 Image of Amazon Rain Forest with stable calibration area marked by rectangle.

have been removed, there can still be a residual fixed bias between the measured  $\sigma_0$  values and the true values. This applies to each of the channels, so there are actually three fixed biases to consider. Normally, we will express these as a fixed absolute bias  $B$ , and two polarimetric ratio biases: A copol ratio bias called  $B_{copol}$  gives the bias in the HH/VV ratio, and a crosspol ratio bias called  $B_{xpol}$  gives the bias in the HH/HV ratio. The values of  $B_{copol}$  and  $B_{xpol}$  can be constrained by using a polarimetric reference target where the HH/VV and HH/HV ratios are known by other means. The best target for this is also the Amazon target area used for long term detrending. PALSAR was able to use corner reflectors to achieve a copol ratio bias of 0.06 dB. Assuming stability of this ratio, the copol ratio measured by SMAP over the same target area can be adjusted to match. The crosspol ratio can also be set to match PALSAR results over the same target area. The expected error for this still needs to be analyzed.

The absolute bias will depend on the final absolute calibration factor applied to the SMAP data. One possibility is to adjust SMAP results to match PALSAR results over the Amazon target area. Since ALOS/PALSAR recently stopped operating, this means assuming that the Amazon target area remains unchanged between now and the SMAP launch in late 2014. Data from the Aquarius mission may also provide a reference to match. Matching SMAP results to another mission effectively adopts the other mission's absolute calibration, which itself may have been derived from other sources. The PALSAR absolute calibration is based on corner reflector cross-sections with a 1-sigma uncertainty of 0.76 dB. Whatever the final value of  $B$  is, it will ultimately be absorbed into the L2 geophysical retrieval algorithms. The active soil moisture algorithm estimates a bias in the L1  $\sigma_0$  values as a part of its fitting procedure.

## 10 Faraday Rotation

Faraday rotation affects L-band signals by rotating the polarization vector during propagation through the ionosphere. This mixes HH, VV, and HV results with each other introducing another source of error. The effect is stronger in daylight hours, so the morning data will suffer less than afternoon data. Furthermore, the SMAP radar is not fully polarimetric so the radar data do not provide a correction by themselves. Instead a correction must be derived from other sources. There are two basic approaches. One is to apply the Faraday correction produced by the radiometer which uses its third Stokes channel to estimate the amount of Faraday rotation. The result is expected to be more than accurate enough to meet the radar error budget for Faraday corrections; however, it will require radar processing to wait for radiometer processing to complete first thus introducing more latency. A variation of this approach would be to incorporate the radiometer faraday correction algo-

rithm (possibly simplified) in the radar L1C processor and compute the correction from the radiometer telemetry data. This variation would add significant development and testing effort to replicate major parts of the radiometer calibration and RFI processing algorithms.

The second approach, which we will adopt for L1 radar processing, is to use estimates of Faraday rotation derived from externally supplied measurements of the ionosphere total electron content (TEC). These measurements are available from several sources (including JPL) on a daily basis. They are based on measurements of GPS signals which also operate at L-band. Since the GPS constellation is located at much higher altitude than SMAP, it sees a more complete integrated TEC than SMAP will see. Based on Aquarius experience, a correction factor of 0.75 is applied to the GPS-based TEC values to account for the shorter atmospheric column seen by SMAP. We assess the impact expected from Faraday rotation on SMAP data using long term models of the ionosphere, and the expected performance of the Faraday rotation correction derived from GPS-based measurements of TEC. The GPS-based measurements supply an estimation of the Faraday rotation angle with an uncertainty (one-sigma) of about 2 degrees. This uncertainty includes a small increase when measurements with 24 hour latency are used instead of near real time measurements that would require a special delivery arrangement. Figures 18 and 19 show cumulative distribution functions (CDF) for the worst case days in a simulation study. The simulation study was based on the planned SMAP orbit and data collection strategy, so the 6pm (descending) half-orbits only collected data North of 45 deg N. latitude, while the 6am (ascending) half-orbits collect data over the whole latitude range and thus show a tail with higher Faraday rotation angles. The median Faraday rotation angle is about 3 degrees for the 6am half-orbits, and about 6 degrees for the 6pm half-orbits.

Propagating the effect of the Faraday rotation angle into the radar backscatter measurements required a land surface backscatter model also used by the L2 retrieval algorithms. Figures 20 - 23 show CDF's of the expected backscatter errors due to a Faraday rotation angle uncertainty of 1.43 degrees (2 degrees scaled by 0.75) for co-pol and cross-pol measurements in the 6am and 6pm half-orbits. Note that the co-pol error budget for Faraday rotation is 0.05 dB and the cross-pol error budget is 0.4 dB. From these plots we see that 3% of the AM co-pol backscatter measurements, and 2% of the AM cross-pol measurements are expected to not meet requirements if no Faraday rotation correction is applied. All of the PM measurements are expected to meet requirements even if no Faraday rotation correction is applied. The PM data show less effect from Faraday rotation because the latitude restriction eliminates the most heavily impacted locations. If a Faraday rotation correction is applied using the GPS-based measurements of TEC, then all measurements are expected to meet the Faraday correction residual error budget.

These results were derived using GPS measurements from 2011 which are sim-

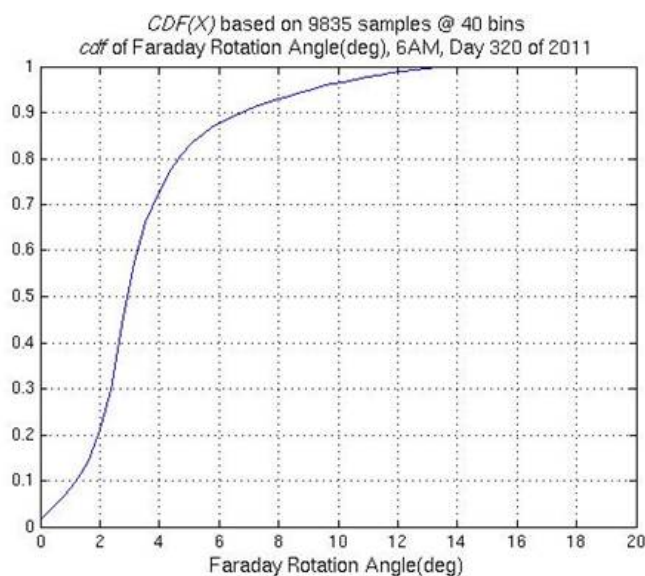


Figure 18: Cumulative distribution function of expected one-way Faraday Rotation angles from GPS based TEC measurements in year 2011. The day with the highest TEC measurements are shown (day of year 320 for 6am).

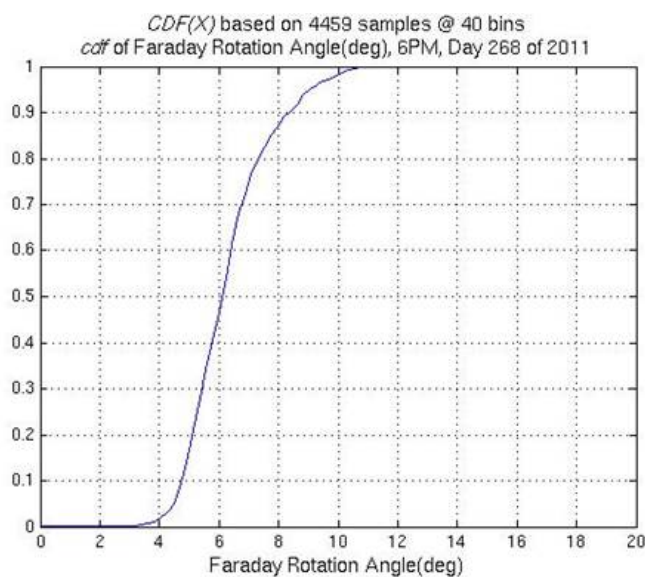


Figure 19: Cumulative distribution function of expected one-way Faraday Rotation angles from GPS based TEC measurements in year 2011. The day with the highest TEC measurements are shown (day of year 268 for 6pm).

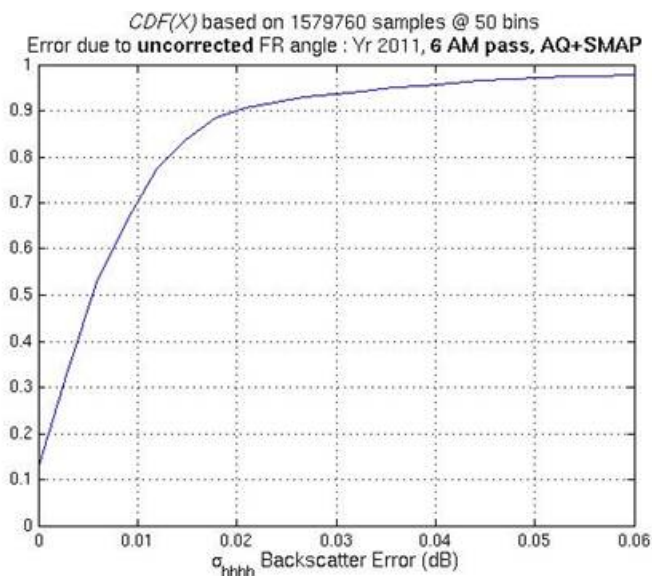


Figure 20: Cumulative distribution function of expected backscatter error (in dB) due to the uncertainty of 1.43 degrees in the measured Faraday rotation angle.

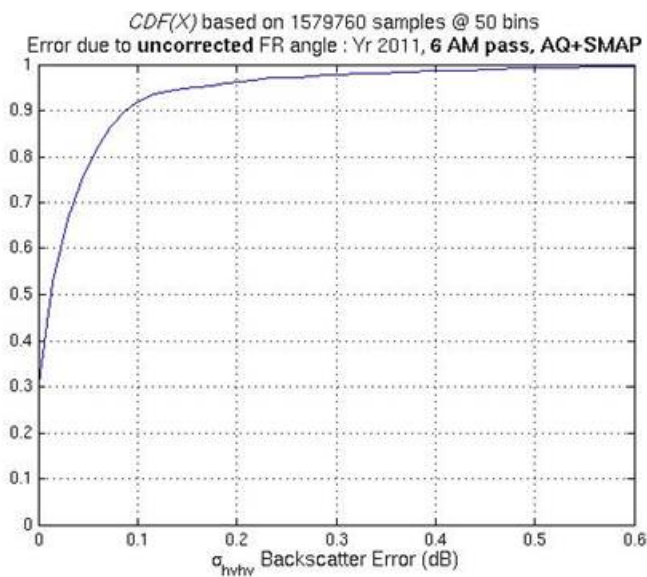


Figure 21: Cumulative distribution function of expected backscatter error (in dB) due to the uncertainty of 1.43 degrees in the measured Faraday rotation angle.

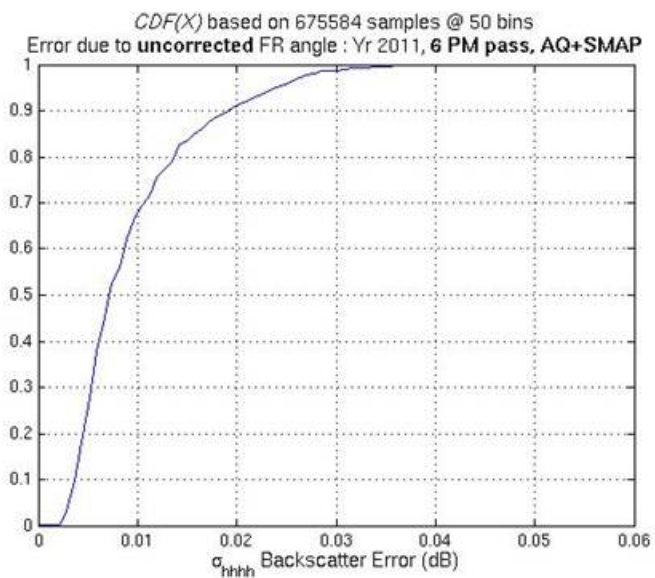


Figure 22: Cumulative distribution function of expected backscatter error (in dB) due to the uncertainty of 1.43 degrees in the measured Faraday rotation angle.

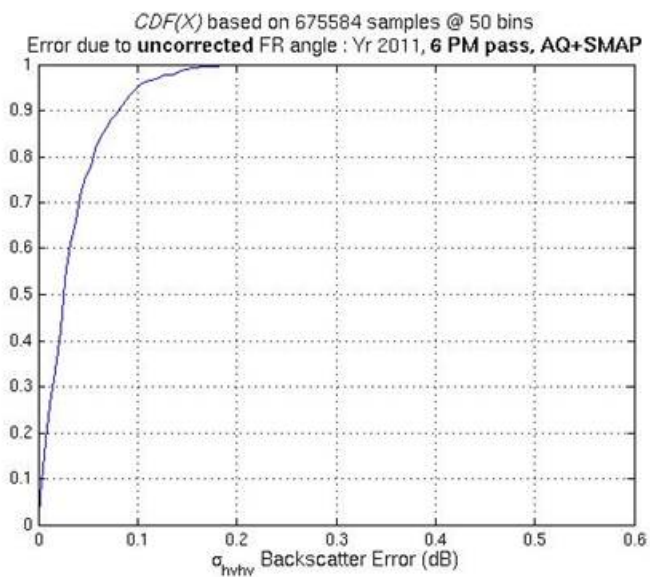


Figure 23: Cumulative distribution function of expected backscatter error (in dB) due to the uncertainty of 1.43 degrees in the measured Faraday rotation angle.

ilar to levels forecast for early in the SMAP mission. The forecast comes from climatology based models that follow the 11 year solar cycle. These models also can provide backup TEC estimates for those occasions when GPS-based measurements are not available. Such interruptions are expected to be rare, and given the low levels of error expected from Faraday rotation effects, will not have a significant impact on data quality. As described later, the SMAP radiometer estimate of Faraday rotation angle will be used to validate the GPS measurement and model based approach.

The assessment study also showed that applying the Faraday rotation correction can increase the errors in areas where the Faraday rotation effect is small due to the uncertainties in the GPS-based measurements. For this reason, the Faraday rotation correction will only be applied when the estimated rotation angle exceeds its own uncertainty. A flag in the LIC product will indicate when the correction is applied.

## **11 RFI**

RFI signals are expected in the L-band frequency window used by the SMAP radar because many other users also operate in this band. Both ground-based sources and space-based sources can cause RFI. A team at JPL has investigated the occurrence, detectability, and correction of RFI signals using operating airborne and space-based L-band radars (such as UAVSAR and ALOS/PALSAR). Results of this study are reported in [16] and [17], and a summary of their analysis is provided in [7]. A condensed version of the summary is provided here along with a description of the baseline RFI detection and correction algorithms planned for L1 processing.

### **11.1 Ground-Based Sources**

The most powerful RFI signals will be from ground-based sources. Data from currently operating airborne and space-based operating L- Band radars (such as UAVSAR and ALOS/PALSAR), and from RFI modeling using the characteristics of know emitters are used to characterize RFI signals. A PALSAR data set comprising collections mostly taken over the U.S., but also including some sites over Europe and Asia, suggests that most observed RFI is from pulsed radars. These data showed 87% of RFI observed from pulsed sources and 13% from other sources including CW. For the most part, sources seem to be relatively narrow band (2-4 MHz). There is some evidence from the PALSAR data to suggest that there are some frequency bands that are globally more clear than others, but no band is completely clear. Characterization studies using PALSAR are by no means comprehensive, and further study is required.

### 11.1.1 Impact of ground-based RFI contamination

When a simulation of RFI from known emitters is performed, approximately 10% of all synthetic aperture intervals can be expected to have interference that exceeds 0.4 dB for co-pol backscatter of -25 dB. This 10% percent value only includes the mechanism where the interference falls directly into the 1 MHz measurement channel. Another mechanism is small signal suppression when a large out-of-band signal saturates the IF stage of the receiver. It is estimated that from 0.1% to 1% of all synthetic apertures will experience at least one event where the receiver saturation produces a 0.4 dB gain compression. These events are expected to be of short duration, and, in an average sense, may not present much of a problem.

### 11.1.2 Detection and correction of ground-based RFI

The evidence is strong that RFI detection and correction will be necessary to meet the science measurement requirement, particularly over North America, Europe, and East Asia. The only detection/correction algorithm that has been demonstrated thus far is the so-called Slow-Time Thresholding or STT algorithm. The STT technique looks at the slow-time series associated with a given range sample, sets an appropriate threshold, and identifies any samples that rise above this threshold as RFI events. The RFI events are simply removed and the data is azimuth compressed without those samples. Studies have indicated that up to 15 azimuth samples can be so excised without generating azimuth side-lobes that cause errors above 0.4 dB. A survey of a limited PALSAR data set shows that the vast majority of scenes have five or fewer RFI events that would be excised by STT, leaving a residual  $\sigma_0$  error of less than 0.1 dB. Other in-band detection schemes have been suggested, but not tested. These include matched detection against known/expected waveform shapes, and statistical analysis of A/D probability distributions. Out-of-band RFI also needs to be considered. Out-of-band effects could be signals which alias into the band of interest, again generating an additive effect; or could be out-of-band signals which saturate the receiver and cause less power to be measured due to small signal suppression. Both of these effects have been observed in PALSAR data. The former (aliasing) effect will be indistinguishable from in-band RFI, and can be detected and removed by the same means. The latter (saturation) effect can be flagged for front-end saturation by the front-end power monitor. There currently is no detector for saturation events in the IF 5 MHz stage, but the 1 MHz signal/noise bands themselves can be used to indicate when high signals are present over most of the band.

## 11.2 Space-Based RFI Sources

In addition to ground-based sources, there is a concern with space-based sources transmitting in L-Band. To date, the only sources that have been identified by Aerospace Corporation as candidates for presenting significant RFI contamination are Global Navigation Satellite Systems (GNSS). The characteristic feature of GNSS is that they emit low, continuous, wide-band interference. This interference is expected to be present globally. The GPS constellation, which operates in the spectral region between 1215-1240 MHz, is believed to create the most interference. This is due primarily to the size and consistency of the constellation. Almost the entire spectral band between 1215 and 1300 MHz, however, is either used or proposed to be used by other GNSS systems (Galileo, GLONASS, COMPASS, etc.).

### 11.2.1 Backlobe Contamination

GNSS interference can enter into the SMAP receiver through direct coupling with the SMAP antenna backlobes. Because the GNSS signals are constant in time (or at least constant over a synthetic aperture time), the interference can basically be treated as a rise in the background noise, analogous to a rise in the thermal noise power. In general, the GNSS interference power is actually several dB below the normal thermal noise power, so it isn't a big effect. Nevertheless, it is a non-negligible effect if not compensated for. The normal noise-only measurement and subsequent noise subtraction step provides a built in technique to remove the contamination. This technique works well where the GPS spectrum is relatively flat (i.e., in the M- and P-Code portions of the spectrum), but does not work well where the spectrum is narrow (i.e., the C-Code portion of the spectrum). It is found that direct GPS interference can be removed to 0.1 dB and 0.2 dB for the lowest co-pol and lowest cross-pol signals respectively if the spectral region around 1227.5 MHz is avoided.

### 11.2.2 Reflection off the Earth

Another mechanism of getting GNSS signal contamination into the SMAP receiver is when these signals reflect off of the Earth. Aerospace Corporation evaluated the statistics of these reflections due to the GPS constellation. The findings were that, whereas the main body of the interference distribution was lower than in the direct broadcast to backlobes case, there were non-negligible probabilities of very large interference signals (much larger than the maximum backscatter signals) when the main beam of the SMAP antenna coincided with specular points on the Earth. The probability of receiving uncorrectable levels of interference due to these specular reflections was about 2% of all the data. Of course, the Earth mostly does not

behave in such a specular fashion, but the L1 processing should nevertheless have the capability of detecting and correcting or flagging these specular reflections.

### **11.3 Summary of RFI Error Assessment**

At this juncture, there is no complete quantitative estimate of the error contribution due to RFI. Such a quantitative estimate would ideally describe the statistics of the residual error after the RFI has been detected and removed during ground data processing. The best that can be said at this point is: under the limitations of the current RFI environment characterizations generated thus far, the allocation in the SMAP error budget of 0.4 dB for RFI seems reasonable, assuming that it is removed using a STT technique during ground processing. In other words, no show stoppers have shown up yet in RFI analyses.

### **11.4 Baseline RFI Removal Algorithm**

The baseline method for RFI mitigation is derived from the STT technique. A moving average filter will first be applied to each range line. The width of the moving average will be specified in the processing configuration file, and may be formulated as a function of scan position and/or orbit position. Smaller widths help to detect short RFI pulses such as those used by some airport surveillance radars. Longer widths help to reduce background noise for longer RFI pulses. Following the range line averaging, a median filter detector will be applied in slow time to identify RFI contaminated samples. The median filter detector has two steps. The first step is to compute the median value over a number of pulses. The number used (ie., the width of the median filter), is another parameter set in the processing configuration file. Again, this width may be formulated as a function of scan position and/or orbit position. The second step is to compare each slow time sample with the median level of the median filter centered on its position. Any samples that rise above the median level by more than a threshold value (also set in the processing configuration file), are flagged as RFI contaminated. The contaminated range line will then have a section of samples centered on the flagged range bin removed and replaced with corresponding samples in the nearest range line with no RFI contamination in the corresponding samples. The number of samples to remove is called the replacement width and is specified in the algorithm parameter file. To avoid adding a bias to the data, random phase noise is applied to the replacement data. If no nearby uncontaminated samples are available within the slow time window width, then the contaminated samples are left unchanged and a RFI corrected flag is set false indicating uncorrectable RFI contamination. These actions are taken for each channel separately, so there are 3 sets of flags (HH,VV, and XPOL). These two flags (contaminated and corrected) are set in the time domain where RFI filtering

occurs, and then passed to the correlation algorithm along with the data. When the data are correlated for particular grid points, The two time domain RFI flags are examined and used to set the spatially organized RFI flags in the output product. The logic is conservative, so if any time domain sample used by a grid point was flagged RFI contaminated, then the grid point RFI contaminated flag is set. If any time domain sample used by a grid point was flagged uncorrectable, the the grid point RFI uncorrectable flag is set. At the conclusion of processing, a QA module adds up the number of occurrences of each flag setting in the spatially organized RFI flags and reports the results in the QA file. A summary of RFI caused data loss is also reported in the PCS metadata file. Note that only uncorrectable grid points are considered lost. Contaminated points that are corrected are not counted as lost. Furthermore, uncorrectable data points are still processed and included in the product. The loss assessment is based on the flags.

In addition to the flagging actions, the number of range samples discarded and the particular range bins affected will be tracked so that an appropriately adjusted statistical error (reported in Kp fields in the output product) can be estimated for output cells that use these data. The baseline algorithm can be executed before or after range compression. Since the SMAP reference functions will not match the RFI sources, it is expected that range compression would spread out the RFI interference by the pulse width, and it makes more sense to do RFI mitigation before range compression. More sophisticated algorithms are possible that involve trying to locate and focus on foreign chirps or tone transmissions. Although these techniques could detect weaker signals than the simple threshold, exploration of these has been postponed currently for budgetary reasons.

## **12 Validation and Test Procedures**

This section looks at how the L1 processing chain will be validated against requirements, and lists some of the expected test procedures. The requirements that apply to L1 processing are listed in table 3.

### **12.1 Pre-Launch**

Before launch, validation will be performed using simulated data to check for expected performance.

#### **12.1.1 Resolution Validation**

The spatial resolution of the SAR data is largely determined by the design of the radar hardware, the design of the antenna, and the orbit altitude. The designed sin-

gle look resolution of the SMAP radar is 236 m in the range direction, and 400-1200 m in azimuth. L1 processing then makes some small tradeoff between the actual processed resolution and some contaminating errors due to ambiguities and multiplicative noise by adjusting the size and shape of the range and azimuth windows applied to the data. Final verification that processed resolution meets requirements will be made by examining the output from simulated point targets positioned at the center and edges of the beam pattern, and repeated around the full conical scan.

### **12.1.2 Radiometric Accuracy Validation**

Validation of the radiometric accuracy of the output L1C image will likely be the most difficult and yet most important task in validating the L1C product. Radiometric validation will start pre-launch with an end to end consistency check. Simulated data with a known backscatter level will be produced for a small amount of time (probably a few scans worth) and then run through the L1C and L1B processors. Results should match within expected statistical limits that are also known. Ideally, the simulation will include many point targets, thus effectively representing a natural distributed target. However, a useful consistency check can also be performed with a single calibrated point target. Alternatively, data from another mission (eg., PALSAR) will be adapted to the SMAP format, and run through the L1B,C processors.

### **12.1.3 Geolocation Validation**

Spatial or geolocation accuracy will be checked pre-launch by comparing the apparent locations of processed simulated point target data against the known locations of the point targets.

## **12.2 Post-Launch**

Immediately following launch the spacecraft and instrument will undergo a three month commissioning period during which the spacecraft will maneuver to the operational orbit, and spin up the antenna. The two instruments will be powered up and checked out during this time. Some cold space viewing will be conducted primarily to aid radiometer calibration, but the radar can also take advantage of data taken during this maneuver. Anytime the beam is pointed at cold space, a two point calibration of receiver gain and noise temperature can be performed using cold space measurements and the internal load measurement subject to some assumptions about the differing signal paths. The calibration preprocessor will be programmed to automatically identify, extract, and process these data along with

other special calibration data. Loopback and associated temperature telemetry processing and modelling can also be performed without valid echo data. Noise channel and receive only data from the radar receivers will be processed and mapped for identification of RFI hot spots.

If valid echo data are collected before the antenna is spun up, there will be an opportunity to process to better than normal azimuth resolution as long as the antenna is generally side-looking. The processing algorithms are designed to automatically exploit longer synthetic aperture times by way of the illuminated area calculation. The operational rectangular algorithm, however, will not properly handle long synthetic apertures. In this case, the direct correlation algorithm would be activated for selected portions of the data take to realize the best azimuth resolution. These data could be very useful for more precise geolocation checks.

After commissioning is completed, a six month L1 cal/val period will begin. During this period the performance and behavior of the radar will be characterized, and appropriate calibration and algorithm parameters will be set in configuration files.

### **12.2.1 Resolution and Signal Processing Validation**

Once data are available from the instrument, the output image from the L1C processor will be examined for proper focussing and performance. The actual resolution obtained can be assessed by looking at sharply defined features such as coastlines and mountains which will also be useful for geolocation verification. Gross problems with focussing should be immediately obvious. The L1C processor will output a single-look image at full resolution to aid in verification and diagnosis of problems. Ambiguity problems can be seen in uniform scenes, especially in the coastal water areas where the backscatter levels will be low. Artifacts in the image such as banding will reveal problems with attitude knowledge, and scan position knowledge. The processing parameters and possibly the algorithms will then be adjusted to minimize the artifacts and problems seen in the single-look images and the output 1-km images.

### **12.2.2 Radiometric Accuracy Validation**

Radiometric accuracy validation can be divided into the reduction of short-term variability coming from the instrument, and vicarious calibration against external reference targets. Short term variations of transmit power and receiver gain are expected due primarily to temperature variations. Pre-launch models based on the loopback data will be constructed and implemented in the calibration preprocessor to supply the L1B and L1C processors with time varying calibration coefficients. During the L1 cal/val period, the performance of the loopback calibration modelling

will be validated by plotting the loopback measurements and the output  $\sigma_0$  results with and without the loopback correction against time and temperature.

Vicarious calibration will be handled by collecting and averaging data in the L1B and L1C processors over stable calibration target areas such as the Amazon, the oceans, and the ice sheets. Assuming that these data are stable, they can be used to track longer term trends in system performance, and to catch other issues such as biases between polarization channels, antenna pointing knowledge errors, RFI, and Faraday rotation effects. Comparisons with Aquarius and PALSAR-2 data (if available) and other instruments will be useful to separate instrument variations from possible scene variations.

### **12.2.3 Geolocation Validation**

Final verification of geolocation will be performed post-launch by looking at high-contrast features with known locations. Coastlines and shorelines should work well and are widely available. Some natural or man-made point-like targets may also work. Specific candidate targets should be identified prior to launch. It may be beneficial to conduct this validation with the high resolution single look image data.

## **13 Acknowledgments**

This work was performed at the Jet Propulsion Laboratory, California Institute of Technology, under contract with the National Aeronautics and Space Administration.

## 14 Acronym List

BFPQ	Block Floating Point Quantizer
CTU	Control and Timing Unit
DEM	Digital Elevation Model
EASE	Equal Area Scalable Earth
FFT	Fast Fourier Transform
FIR	Finite Impulse Response
FM	Frequency Modulated
FPGA	Field Programmable Gate Array
GNSS	Global Navigation Satellite System
GPS	Global Positioning System
GSFC	Goddard Space Flight Center
HDF	Hierarchical Data Format
IF	Intermediate Frequency
JPL	Jet Propulsion Laboratory
NAIF	Navigation and Ancillary Information Facility
NASA	National Aeronautics and Space Administration
NOAA	National Oceanographic and Atmospheric Administration
NRC	National Research Council
NRCS	Normalized Radar Cross Section
PRF	Pulse Repetition Frequency
PRI	Pulse Repetition Interval
RF	Radio Frequency
RFI	Radio Frequency Interference
SAR	Synthetic Aperture Radar
SCH	along track, cross track, height coordinates
SMAP	Soil Moisture Active Passive - Mission name
SPECAN	Spectral Analysis
SPICE	Files used by the NAIF toolkit
SRTM	Shuttle Radar Topography Mission
STALO	Stable Local Oscillator
STT	Slow Time Threshold
USGS	United States Geological Survey

## References

- [1] National Research Council, "Earth Science and Applications from Space: National Imperatives for the Next Decade and Beyond," pp. 400, 2007.
- [2] D. Entekhabi et al., "The Hydrosphere State (HYDROS) mission concept: An earth system pathfinder for global mapping of soil moisture and land freeze/thaw," *IEEE Trans. Geosci. Remote Sens.*, vol 42, no. 10, pp. 2184-2195, Oct 2004.
- [3] D. Entekhabi et al., "The Soil Moisture Active Passive (SMAP) Mission," *Proceedings of the IEEE*, vol 98, no. 5, pp. 704-716, May 2010.
- [4] E. Podest, "SMAP Ancillary Data Report: Digital Elevation Model," JPL D-53056, 2011.
- [5] S. Hensley et al., "Jurassicprok A Dual Frequency Radar Interferometric Processor Developed for the GeoSAR Program," Algorithm Description Document, March 2003, JPL/CalTech.
- [6] M. Spencer et al., "High-Resolution Measurements With a Spaceborne Pencil-Beam Scatterometer Using Combined Range/Doppler Discrimination Techniques," *IEEE Trans. on Geo. and Remote Sens.*, vol 41, no. 3, pp. 567-581, 2003.
- [7] S. Chan and M. Spencer, "Soil Moisture Active Passive (SMAP) Project: Radar Error Budget," JPL-D-61622, April 20, 2011.
- [8] F. Ulaby et al., *Microwave Remote Sensing, Vol II*, Addison-Wesley Publishing Co, 1982.
- [9] R. Kwok and W.T.K. Johnson, "Block Adaptive Quantization of Magellan SAR Data," *IEEE Trans. on Geo. and Remote Sens.*, vol 27, no. 4, pp. 375-383, 1989.
- [10] M. Spencer et al., "Improved Resolution Backscatter Measurements with the SeaWinds Pencil-Beam Scatterometer," *IEEE Trans. on Geo. and Remote Sens.*, vol 38, no. 1, pp. 89-104, 2000.
- [11] M. Shimada, "Long term stability of L-band normalized radar cross-section of Amazon rainforest using the JERS-1 SAR," *Can. J. Remote Sensing*, Vol 31, No. 1, pp. 132-137, 2005.
- [12] J. Curlander and R. McDonough, *Synthetic Aperture Radar*, John Wiley and Sons, Inc, 1991.

- [13] F. Ulaby et al., *Microwave Remote Sensing, Vol I*, Addison-Wesley Publishing Co, 1981.
- [14] N. Pierdicca et al., "The Calibration of the Envisat Radar Altimeter Receiver by a Passive Technique," *IEEE Trans. on Geo. and Remote Sens.*, vol 44, no. 11, pp. 3297-3307, 2006.
- [15] I. Cumming and F. Wong, *Digital Processing of Synthetic Aperture Radar Data*, Artech House Inc., 2005.
- [16] J. E. Belz et al., "A Study of Radio Frequency Interference in the Space-to-Earth Exploration Allocation at L-Band," *Proceedings of the IEEE Aerospace Conference*, Big Sky, MT, 2011.
- [17] S. Chan and M. Spencer, "RFI Study for the SMAP Radar," *Proceedings of the IEEE Radar Conference*, Pasadena, CA, May, 2009.